

# Ash3d: A finite-volume, conservative numerical model for ash transport and tephra deposition

Hans F. Schwaiger,<sup>1</sup> Roger P. Denlinger,<sup>2</sup> and Larry G. Mastin<sup>2</sup>

Received 26 October 2011; revised 19 February 2012; accepted 25 February 2012; published 17 April 2012.

[1] We develop a transient, 3-D Eulerian model (Ash3d) to predict airborne volcanic ash concentration and tephra deposition during volcanic eruptions. This model simulates downwind advection, turbulent diffusion, and settling of ash injected into the atmosphere by a volcanic eruption column. Ash advection is calculated using time-varying pre-existing wind data and a robust, high-order, finite-volume method. Our routine is mass-conservative and uses the coordinate system of the wind data, either a Cartesian system local to the volcano or a global spherical system for the Earth. Volcanic ash is specified with an arbitrary number of grain sizes, which affects the fall velocity, distribution and duration of transport. Above the source volcano, the vertical mass distribution with elevation is calculated using a Suzuki distribution for a given plume height, eruptive volume, and eruption duration. Multiple eruptions separated in time may be included in a single simulation. We test the model using analytical solutions for transport. Comparisons of the predicted and observed ash distributions for the 18 August 1992 eruption of Mt. Spurr in Alaska demonstrate to the efficacy and efficiency of the routine.

**Citation:** Schwaiger, H. F., R. P. Denlinger, and L. G. Mastin (2012), Ash3d: A finite-volume, conservative numerical model for ash transport and tephra deposition, *J. Geophys. Res.*, 117, B04204, doi:10.1029/2011JB008968.

## 1. Introduction

[2] Among the many hazards associative with volcanic eruptions, the transport of tephra in the atmosphere can have far-reaching consequences. The fine-grained fraction of tephra (volcanic ash) can be widely dispersed and can lead to a degradation of air quality. Even in small quantities the presence of airborne ash poses a significant risk for aircraft. Exposure of aircraft to ash can result in extensive damages to windshields, electrical and hydraulic systems, blocking of pitot tubes, and leads to engine malfunction and failure [Casadevall, 1994; Peterson and Dean, 2008; Sparks *et al.*, 1997].

[3] Prior to the April-May 2010 eruptions of Eyjafjallajökull in Iceland, airlines had typically adopted a zero-tolerance policy regarding airborne volcanic ash in which flights were restricted or canceled if any ash was predicted or observed. During the Iceland eruption, the costly shutdown of airspace over Europe led to the adoption in Europe of maximum ash-concentration levels through which jet engines can safely fly (GE Aviation, All operators wire: Subject: Engine operation—Volcano Eyjafjallajökull, 2010).

[4] In recent years there have been significant advances in the identification of volcanic ash through both ground-based

[Dacre *et al.*, 2011] and satellite observations [Prata, 2009; Pavoloni, 2010]. These observations provide snapshots of ash cloud concentration downwind and are essential for supporting ash forecasts. However, satellite data are limited to the highest visible layer. Meteorological clouds obscure ash clouds beneath them, and multiple ash layers may develop; both factors compromise satellite measurements. Furthermore, satellites can provide timely observations of where airborne ash is currently located, but hazard assessments require forecasting. Consequently, numerical estimation of ash distribution using known wind fields must accompany satellite estimates of ash concentration if we are to accurately predict ash cloud evolution.

[5] The numerical simulation of the advection, dispersion and deposition of the contaminant or particle plumes has progressed in recent years and uses several methods that are broadly characterized by their numerical framework (Eulerian versus Lagrangian). Operational simulations such as those conducted by the Volcanic Ash Advisory Centers (VAACs), typically employ Lagrangian, particle-based formulation (e.g., Puff [Searcy *et al.*, 1998], HYSPLIT [Draxler and Hess, 1997], NAME [Jones *et al.*, 2007], MDLPO [D'Amours and Malo, 2004], FLEXPART [Stohl *et al.*, 2005], Vol-CALPUFF [Barsotti *et al.*, 2008]). These models calculate the evolution of an ash cloud by integrating the trajectory of a set of particles (or puffs) and advecting them along streamlines. This Lagrangian class of models has several advantages for operational runs in that they typically are less computationally intensive and exhibit much less numerical diffusion than Eulerian calculations. Computational

<sup>1</sup>Alaska Volcano Observatory, U.S. Geological Survey, Anchorage, Alaska, USA.

<sup>2</sup>Cascades Volcano Observatory, U.S. Geological Survey, Vancouver, Washington, USA.

expense scales linearly with the number of particles used and the code structure is typically more amenable to parallelization. However, in Lagrangian models, total mass loading and absolute concentrations are typically calculated from the number density of the particles and can exhibit reduced accuracy in regions where the number density of the particles is low. Eulerian formulations do not exhibit this loss of accuracy.

[6] Operational models which employ an underlying Eulerian grid include MOCAGE [Josse et al., 2004], used at the Toulouse VAAC, ATHAM [Oberhuber et al., 1998], and Fall3d [Armienti et al., 1988; Costa et al., 2006; Folch et al., 2009], which uses an explicit, finite difference scheme. These models calculate the evolution of the concentration of ash at every point in the model domain, resulting in a more direct calculation of absolute concentration than is done in Lagrangian models.

[7] Another class of models is based on analytic expressions for tephra deposition. Examples include HAZMAP [Macedonio et al., 2005; Connor et al., 2001], and Tephra2 [Bonadonna et al., 2005], which typically simplify the wind field sufficiently for tephra thickness to be described by an explicit mathematical expression. Since no numerical integration is required for this class of models, these programs can execute faster than either the Lagrangian or Eulerian advection-diffusion models.

[8] Finally, volcanic ash tracking has recently been added to a few sophisticated numerical weather prediction models. A few studies have recently been conducted modeling tephra using REMOTE [Langmann et al., 2009, 2010], COAMPS [Westphal et al., 2008] and the Weather Research and Forecasting model (WRF-CHEM) [Steenes et al., 2010]. In a class by itself, these models typically require supercomputing resources and can simulate the full dynamics of the atmosphere, including any coupling with volcanogenic effects (ash-loading, SO<sub>2</sub> emissions).

[9] With the continuing rapid advancement of computing resources, three-dimensional calculations using a fixed Eulerian framework are becoming more tractable for operational calculations on global grids as well as for research investigations. Hence, we decided to emphasize accuracy over speed and develop a new Eulerian tephra advection and dispersion model, Ash3d, based on a finite-volume numerical scheme. This model is designed to be used both in an operational setting, using fast numerical schemes and simplifying assumptions, as well as in research investigations, where more careful attention is required for the strict adherence to conservation laws or a richer set of atmospheric conditions.

[10] This paper is organized as follows. Section 2 describes the underlying equations. We then describe the methodologies to calculate these equations in section 3. In section 4, we present the performance of the methods for several test cases, quantifying the effects of numerical diffusion and showing convergence behavior. Validation of the model is presented in section 5 using data for the 18 August 1992 eruption of the Crater Peak vent of Mt. Spurr in Alaska. This eruption is particularly well observed with satellite observations as well as tephra deposits.

## 2. Model Formulation

[11] To forecast the trajectory of an ash cloud and to predict the likely area affected by it, Ash3d solves for mass

conservation in the atmosphere, allowing for turbulent diffusion and for settling of tephra during transport. Input parameters are the meteorological conditions (wind velocity, pressure, temperature, moisture variables), and the volcanic source conditions that inject ash into the atmosphere. The meteorological condition of utmost importance is the wind field, which is provided either by transient, 3-D numerical weather forecasts, or by 1-D vertical sonde profiles in cases where access to 3-D wind fields is limited or in conflict with known local conditions.

### 2.1. Advection

[12] If we assume that in any arbitrary volume of air, the volume of tephra is insignificant relative to the volume of air, conservation of mass may be written in terms of tephra concentration,  $q$ , or mass per unit volume. In conservative form this is given by

$$\frac{\partial q}{\partial t} + \nabla \cdot ((\mathbf{u} + \mathbf{v}_s)q) = 0 \quad (1)$$

where  $q$  is the concentration of a particular grain size,  $\mathbf{u}$  is the velocity field,  $\mathbf{v}_s$  is the settling velocity of the ash particles. Notation is given in the notation section. The total concentration of the ash cloud is composed of ash described by an arbitrary number of grain sizes, in which the advection of each grain size is calculated independently. Though there is a growing recognition of the importance of particle aggregation within ash plumes, in which smaller particles collide and adhere to one another and effectively create larger particles [Bonadonna et al., 2011], the effects of aggregation and any interaction among grain sizes are neglected.

### 2.2. Turbulent Diffusion

[13] Following gradient transport theory ( $K$ -theory) [Jacobson, 2005, p. 72], velocity and concentration can be expressed as

$$u = \bar{u} + u' \quad (2)$$

$$q = \bar{q} + q' \quad (3)$$

where  $\bar{u}$  denotes an ensemble average value of  $u$ , and  $u'$  denotes a perturbation. Kinematic turbulent fluxes can be parameterized as proportional to the gradient of the fluctuating variable.

$$\overline{u'q'} = -K_x \frac{\partial \bar{q}}{\partial x} \quad (4)$$

Substituting these expressions into equation (1) leads to a diffusion term in the advection equation where  $K_x$  is the diffusivity in the  $x$ -direction, with analogous equations for diffusion in the  $y$  and  $z$  directions. This diffusivity can be spatially variable and can be a function of the local meteorological conditions. We treat diffusivity as a constant.

### 2.3. Deposition

[14] The removal of airborne tephra and the deposition onto the ground surface is a result of several mechanisms, including sedimentation, dry deposition, washout and rainout. The last two terms refer to the wet removal from in-cloud scavenging

and below-cloud scavenging, respectively [chap. 20 *Seinfeld and Pandis*, 2006]. Ash3d calculates the accumulation of deposits via sedimentation. The calculation of wet deposition due to rainout is currently being developed and will be presented in a subsequent paper. Deposits are calculated by tracking the flux of ash onto topography, and output as mass per unit area (mpua). The full grain size distribution of the accumulated deposit is preserved and can be used to compare to observed samples. If the deposit thickness is needed, it is estimated by assuming a deposit density, typically  $\rho_d = 1000 \text{ kg/m}^3$  in our model runs.

[15] The fall velocity of a particular grain size,  $v_s$ , can be specified as a constant in the input file for Ash3d, or it can be calculated explicitly using atmospheric conditions. Ash3d uses the terminal settling velocity given by *Bird et al.* [1960, p. 182].

$$v_s = \sqrt{\frac{4d\rho g}{3C_d\rho_a}} \quad (5)$$

where  $C_d$  is a drag coefficient,  $d$  is the particle diameter,  $\rho_a$  is the density of air, and  $g$  is the acceleration of gravity. Several models estimate the drag coefficient  $C_d$ , for non-spherical particles [*Wilson and Huang*, 1979; *Suzuki*, 1983; *Pfeiffer et al.*, 2005; *Ganser*, 1993; *Dahneke*, 1973; *Chen et al.*, 1993]. Ash3d uses the empirical expression given for volcanic ash particles by *Wilson and Huang* [1979], in which  $C_d$  is a function of the particle's shape.

$$C_d = \frac{24}{Re} F^{-0.828} + 2\sqrt{1.07 - F} \quad (6)$$

In the above equation,  $F$  is a shape parameter for an ellipsoidal particle defined as the ratio of the average of the minor axes to the major axis of the particle:  $(b + c)/2a$ .  $Re$  is the particle Reynolds number given by *Wilson and Huang* [1979, equation 4].

$$Re = \frac{v_s \rho_a d}{\eta_a} \quad (7)$$

[16] The density of air,  $\rho_a$ , is calculated via the ideal gas law using local pressure and temperature. Air viscosity,  $\eta_a$ , is calculated via Sutherland's Law [*Jacobson*, 2005, equation 4.54]. In some circumstances, fine ash particles can be small enough that the mean free path length of an air molecule,  $\lambda_a$ , is on a similar scale to the particle's size. This is characterized by the Knudsen number,  $Kn = 2\lambda_a/d$ . In these high  $Kn$  conditions, non-continuum effects must be taken into account by scaling the drag coefficient by the Cunningham slip-correction factor [*Seinfeld and Pandis*, 2006, equation 9.34]. This is typically used to modify Stokes' Law for spherical particles by scaling the drag coefficient by  $1/C_C$  where

$$C_c = 1 + Kn \left[ \alpha + \beta \exp\left(-\frac{\gamma}{Kn}\right) \right] \quad (8)$$

For ellipsoidal particles, equation (8) must be adjusted by scaling  $Kn$  according to *Dahneke* [1973, Table 1]. We use

values for the empirical coefficients  $\alpha$ ,  $\beta$ , and  $\gamma$  given by *Seinfeld and Pandis* [2006, equation 9.34]. The air mean free path,  $\lambda_a$ , is given by *Seinfeld and Pandis* [2006, equation 9.6]:

$$\lambda_a = \frac{2\eta_a}{P \sqrt{8M_B/\pi RT}} \quad (9)$$

Equation (6) was empirically determined from fall data from volcanic particles in the size range  $30 \mu\text{m} < d < 1500 \mu\text{m}$ . The slip-flow correction only becomes significant for particles smaller than this range. Figure 1 shows the fall velocity models as a function of particle size for prolate ellipsoidal particles ( $F = 0.4$ ) as well as for more equant particles ( $F = 0.8$ ) using atmospheric conditions at a height of 10 km. The Ganser model is also shown for comparison. The Wilson and Huang model predicts slightly slower settling velocities than the Ganser model and the Stokes' model (by 53% and 17% for  $F = 0.4$  and  $F = 0.8$ , respectively). For  $F = 0.4$ , the slip-flow corrections are minor, however for  $F = 0.8$ , it leads to increases in fall velocities by 2%, 21%, and 348% for  $d = 10 \mu\text{m}$ ,  $1 \mu\text{m}$  and  $0.1 \mu\text{m}$  respectively. *Rose and Durant* [2009] calculated that ash in this size range can be a significant component (30% to >50%) of the total grain size distribution and noted that sedimentation rates are observed to be much faster than that predicted by Stokes' Law.

## 2.4. Source Terms

[17] The source term,  $S$ , denotes the rate of mass influx per unit volume per unit time into the ash plume (e.g.,  $\text{kg/m}^3 \text{s}$ ). It results from a volcanic eruption and is specified by assigning a vertical concentration profile to the column of computational cells at the vent location. The parameters specifying this profile are the height of the plume, the start time and duration of the plume, and the total mass erupted during that event. Volcanic eruptions are seldom sustained and their transient behavior, coupled with the wind, has a significant influence on the distribution of airborne ash concentrations [*Mastin et al.*, 2010]. When ground observations provide information on the transient variation of plume height, this information is input into Ash3d as a series of consecutive individual plumes (eruptions). When the vertical ash loading for a plume is not known, operational models often characterize the plume with a linear distribution of ash [*Webster et al.*, 2012]. To provide greater flexibility in describing the vertical ash distribution, Ash3d characterizes plumes with a Suzuki distribution [*Suzuki*, 1983; *Carey*, 1996], or

$$\frac{dS}{dz} = S \frac{k^2(1-z/H)\exp[k(z/H-1)]}{H[1-(1+k)\exp(-k)]} \quad (10)$$

This equation describes a family of curves for a plume height,  $H$ , and erupted mass at a given time step,  $S$ , with a mass distribution over height that is controlled by  $k$ . Low values of  $k$  lead to a more uniform distribution of mass with height, whereas higher values concentrate more of the mass near the top. The maximum concentration occurs at  $z = H(k-1)/k$ .

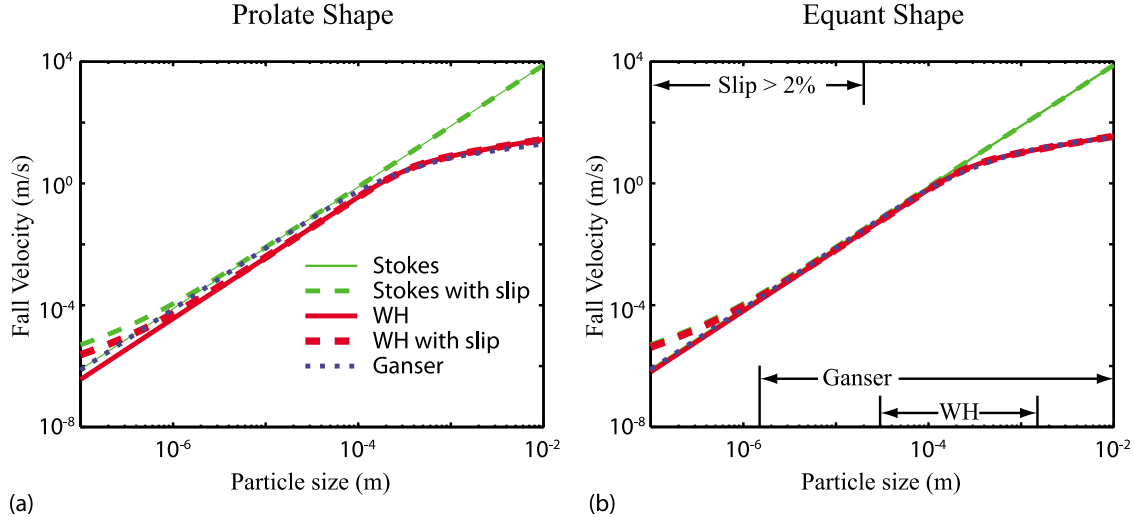


**Figure 1.** (a and b) Comparison of fall velocity models of Stokes, WH [Wilson and Huang, 1979] and Ganser [1993]. Corrections due to slip-flow to the Stokes and WH models are shown in dashed lines. Atmospheric conditions used in calculating terminal velocities and mean free paths lengths are  $T = -57.1^\circ\text{C}$  and  $P = 250$  mb. These are the conditions measured at 10.3 km in Anchorage on 18 August 1992. Figure 1a shows Ganser and WH fall velocities for prolate particles ( $a = 1.0$ ,  $b = 0.4$ ,  $c = 0.4$ ), while Figure 1b shows velocities for more equant particles ( $a = 1.0$ ,  $b = 0.8$ ,  $c = 0.8$ ). In both plots, Stokes velocities are for spherical particles. Velocity increases due to Cunningham slip are less pronounced at lower elevations. Figure 1b shows the range of particle sizes used in constraining the WH and Ganser models.

## 2.5. Governing Equations

[18] Combining the advection equation (equation (1)) with the formulation for turbulent diffusion, fall velocity and tephra sources leads to the following governing equation.

$$\frac{\partial q}{\partial t} + \nabla \cdot [(\mathbf{u} + \mathbf{v}_s)q] - \nabla \cdot (\mathbf{K} \nabla q) = S \quad (11)$$

## 3. Numerical Implementation

[19] The governing equation (equation (11)) can be expanded.

$$\begin{aligned} \frac{\partial q}{\partial t} &= S - \left[ \frac{\partial}{\partial x}(uq) - \frac{\partial}{\partial y}(vq) \right] - \left[ \frac{\partial}{\partial z}(w + v_s)q \right] \\ &+ \frac{\partial}{\partial x} \left( K_x \frac{\partial q}{\partial x} \right) + \frac{\partial}{\partial y} \left( K_y \frac{\partial q}{\partial y} \right) + \frac{\partial}{\partial z} \left( K_z \frac{\partial q}{\partial z} \right) \end{aligned} \quad (12)$$

[20] The numerical strategy is to use the method of fractional steps [Durran, 1999] in which equation (12) is decomposed into the following sequence of steps which integrate  $q$  from time step  $n$  to time step  $n + 1$ . Time steps are denoted as superscripts.

$$q^* = q^n + \Delta t S^n \quad (13)$$

$$q^{**} = q^* - \Delta t \left[ \frac{\partial}{\partial x}(uq^*) + \frac{\partial}{\partial y}(vq^*) \right] \quad (14)$$

$$q^{***} = q^{**} - \Delta t \frac{\partial}{\partial z} [(w + v_s)q^{**}] \quad (15)$$

$$q^{n+1} = q^{***} + \Delta t [\nabla \cdot (\mathbf{K} \nabla q^{***})] \quad (16)$$

Effectively, although all processes (source insertion, advection, sedimentation, diffusion) are coupled throughout the time step, numerically they are treated separately. This separate and sequential treatment introduces a small splitting error into the solution if the velocities are spatially varying. Furthermore, each of these processes is calculated using numerical techniques that introduce small errors that accumulate as the simulation progresses. Often there is a trade-off between the quality of the solution (in terms of error) and the speed of execution. In this section, we outline and compare different numerical techniques we have implemented in Ash3d to solve equations (13)–(16).

[21] Equation (13) is shown here as a first-order Forward Euler integration because we treat source terms as constant in time over an eruption interval. Transient eruption source parameters are approximated by a series of sequential constant intervals. There are many techniques that can be used to solve the advection steps (equations (14) and (15)). We have implemented and tested three techniques that have various advantages and disadvantages. They are the Donor-cell upwind with dimension-splitting (DCU), Corner-transport upwind (CTU) and the semi-Lagrangian technique. Each is based on a finite-volume discretization of the domain and is shown schematically in Figure 2. The DCU method applies a 1-D high-resolution Lax-Wendroff method in each dimension sequentially. The CTU method, in contrast, solves the multiple dimensional equation in a single step, but can be more computationally burdensome. The semi-Lagrangian method is fast, but can result in lack of mass conservation. The reason we have implemented several numerical techniques is so that the software can be adjusted for use in research applications in which the highest quality solution is desired, as well as in operational

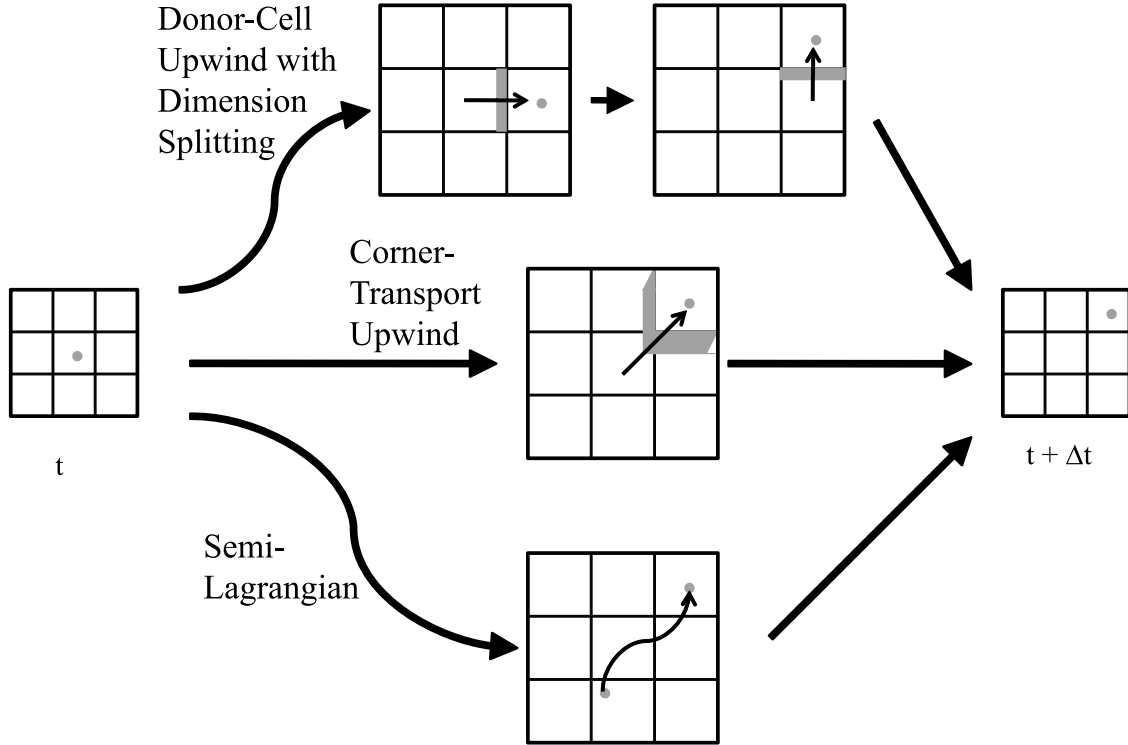


**Figure 2.** Schematic of the three numerical techniques implemented in the software: Donor-Cell Upwind with dimension-splitting (DCU), Corner-Transport Upwind (CTU), semi-Lagrangian.

settings, in which adequate solutions are needed in the fastest time possible.

### 3.1. Finite-Volume

[22] We apply a variant of the Lax-Wendroff method to the conservative form of the advection equation by replacing terms of the Taylor series expansion (in  $t$ ) with spatial derivatives derived from the governing equation.

$$\frac{\partial q}{\partial t} = -\nabla \cdot (\mathbf{u}q) \quad (17)$$

$$\begin{aligned} \frac{\partial^2 q}{\partial t^2} &= -\nabla \cdot \left( \frac{\partial \mathbf{u}}{\partial t} q + \mathbf{u} \frac{\partial q}{\partial t} \right) \\ &\approx \left[ (\nabla \cdot \mathbf{u})^2 + \mathbf{u} \cdot [\nabla(\nabla \cdot \mathbf{u})] \right] q \\ &\quad + [2(\nabla \cdot \mathbf{u})\mathbf{u} + \mathbf{u} \cdot \nabla \mathbf{u}] \cdot \nabla q + [\mathbf{u} \otimes \mathbf{u}] : \nabla \nabla q \end{aligned} \quad (18)$$

In equation (18), we assume transient changes in  $\mathbf{u}$  are small compared to the magnitude of  $\mathbf{u}$ . Inserting the above expressions for the time derivatives of  $q$  into a Taylor series and considering just the  $x$ -dimension leads to the following expression.

$$\begin{aligned} q^{n+1} &= q^n - \Delta t \left[ \frac{\partial u}{\partial x} q + u \frac{\partial q}{\partial x} \right] \\ &\quad + \frac{1}{2} \Delta t^2 \left[ \left( \frac{\partial u}{\partial x} \right)^2 + \frac{\partial^2 u}{\partial x^2} u \right] q + \left( 3 \frac{\partial u}{\partial x} u \right) \frac{\partial q}{\partial x} + u^2 \frac{\partial^2 q}{\partial x^2} + \dots \end{aligned} \quad (19)$$

This one-dimensional simplification removes all cross-derivative terms. For the finite-volume discretization of this

equation, we use a flux-difference splitting formulation [LeVeque, 2003, equation 4.4] which prescribes the update to the average concentration in a cell  $i, j, k$  at time  $n$  (denoted  $Q_{i,j,k}^n$ ) to time  $n + 1$ .

$$Q_{i,j,k}^{n+1} = Q_{i,j,k}^n - \frac{\Delta t}{\Delta \kappa} \left( F_{i+1/2,j,k}^n - F_{i-1/2,j,k}^n \right) \quad (20)$$

The fluxes,  $F_{i \pm 1/2,j,k}^n$ , refer to fluxes in the  $i$ -direction ( $x$  for Cartesian and  $\lambda$  for spherical grids) of tephra across the cell interfaces at  $i \pm 1/2$ . The areas of these interfaces are denoted  $\sigma_{i \pm 1/2}$ , and the cell volume is denoted  $\Delta \kappa$  (Figure 3a). In Cartesian coordinates,  $\Delta \kappa$  is simply the product of  $\Delta x$ ,  $\Delta y$  and  $\Delta z$ . In spherical coordinates, the cell volume is a function of position and can be expressed as follows.

$$\Delta \kappa = \frac{1}{3} (\lambda_2 - \lambda_1) (r_2^3 - r_1^3) (\cos \phi_1 - \cos \phi_2) \quad (21)$$

where  $\lambda$ ,  $\phi$ , and  $r$  are the latitude, longitude and radius (see Figure 3a). For a full update to a cell's concentration based on the volumetric averages of the fluxes in all directions, fluxes in  $j$  and  $k$  must also be included using equations similar to equation (20).

[23] Many numerical weather prediction simulations for North America use projected grids, such as those produced by NCEP at NOAA, while global forecast models generally use a spherical coordinate system. We will keep the equations general; however, the numerical implementation of the equations simplifies significantly when  $\sigma$  and  $\Delta \kappa$  are not functions of position.

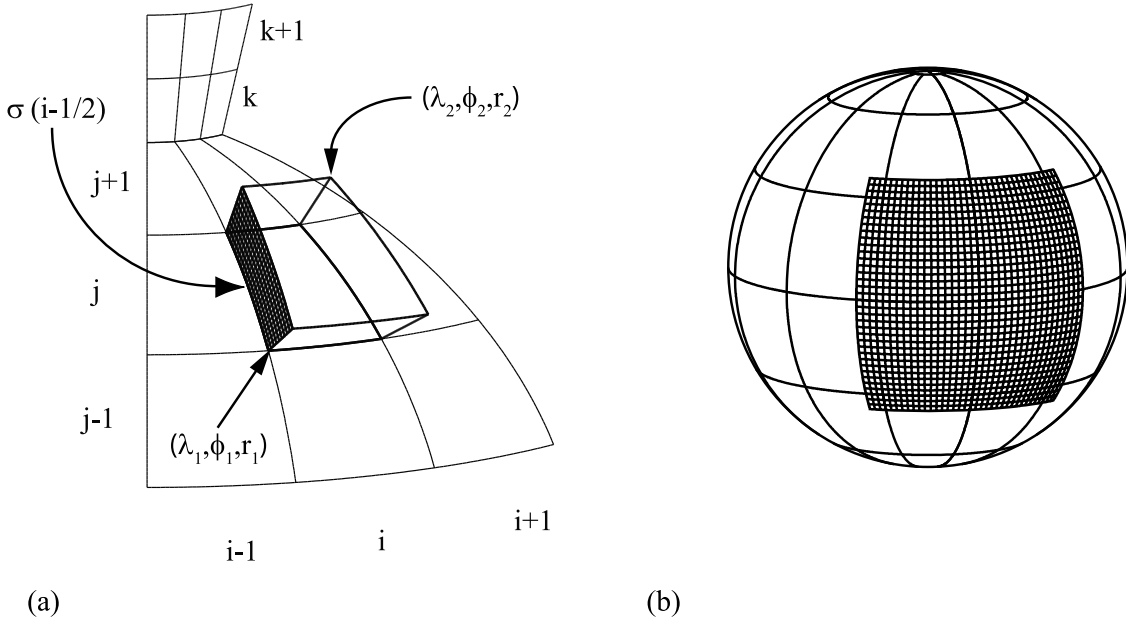


**Figure 3.** (a) A generalized cell of volume  $\Delta\kappa$  and with surfaces  $\sigma$ . Coordinates used in the volume calculation (equation (21)) are shown. (b) The low resolution grid ( $2^\circ$ ) used in the longitude/latitude grid convergence studies. Refined grids are at  $1^\circ$ ,  $0.5^\circ$  and  $0.25^\circ$  in both latitude and longitude. The grid extents are  $-36^\circ \leq \phi \leq 36^\circ$ ,  $-36^\circ \leq \lambda \leq 36^\circ$ .

[24] Equation (20) can be written in fluctuation form [LeVeque, 2003, equation 6.59]:

$$\begin{aligned} Q_{i,j,k}^{n+1} = & Q_{i,j,k}^n - \frac{\Delta t}{\Delta\kappa} (\mathcal{A}^- \Delta Q_{i+1/2,j,k} + \mathcal{A}^+ \Delta Q_{i-1/2,j,k}) \\ & - \frac{\Delta t}{\Delta\kappa} (\tilde{F}_{i+1/2,j,k} - \tilde{F}_{i-1/2,j,k}) \end{aligned} \quad (22)$$

where  $\mathcal{A}^\pm$  are the fluctuations, the net contribution of right-propagating and left-propagating effects due to the differences in  $Q$  at  $i - 1/2$ .  $\tilde{F}$  are the higher-order corrections to the flux (such as a Lax-Wendroff correction). As with equation (20), equation (22) is written only for the  $i$ -direction ( $x$  or  $\lambda$ ). Equations for the  $j$  and  $k$  directions are analogous.

### 3.1.1. Donor-Cell Upwind

[25] A simple finite-volume implementation of the conservative form of the advection equation is the Donor-cell upwind method described by LeVeque [1996, 2003]. With this method, we essentially apply a high-resolution method along each coordinate dimension sequentially. For the horizontal advection equation, first one coordinate direction is integrated according to LeVeque [2003, equation 19.19], followed by the second horizontal direction. Since each dimension is considered in isolation, the following equations only include subscripts in  $i$ .

[26] For a spatially varying velocity, the fluctuations can be expressed as follows.

$$\mathcal{A}^+ \Delta Q_{i-1/2} = (u\sigma)_{i-1/2}^+ (Q_i - Q_{i-1}) + [(u\sigma)_{i+1/2}^- - (u\sigma)_{i-1/2}^-] Q_i \quad (23)$$

$$\mathcal{A}^- \Delta Q_{i-1/2} = (u\sigma)_{i-1/2}^- (Q_i - Q_{i-1}) + [(u\sigma)_{i+1/2}^+ - (u\sigma)_{i-3/2}^+] Q_i \quad (24)$$

In the above equations,  $(u\sigma)_{i-1/2}^+$  refers to the product of the normal velocity at interface  $i - 1/2$  (shaded surface in Figure 3) and the surface area of that interface. The superscript + or - denotes the right- and left-propagating contributions (i.e., if  $u < 0$  then  $(u\sigma)^+ = 0$ ). The fluctuations are the upwind discretization of  $\nabla \mathbf{u} q + \mathbf{u} \cdot \nabla q$  (first-order terms of equation (19)). A higher-order (Lax-Wendroff) correction can be applied using the following form for  $\tilde{F}$ .

$$\tilde{F}_{i-1/2} := \frac{1}{2} \left| (u\sigma)_{i-1/2} \right| \left( 1 - \frac{\Delta t}{\Delta\kappa} \left| (u\sigma)_{i-1/2} \right| \right) \widetilde{\Delta Q}_{i-1/2} \quad (25)$$

This correction provides the centered approximation to the  $[\mathbf{u} \otimes \mathbf{u}] : \nabla \nabla q$  term of equation (18), or the  $u^2 \partial^2 q / \partial x^2$  term of equation (19). Essentially, we are including  $\partial u / \partial x$  in the first-order term, but not in the second-order term. This is only valid when  $\partial u / \partial x$  is small.  $\widetilde{\Delta Q}_{i-1/2}$  is the limited version of the concentration difference at the  $i - 1/2$  interface in which minmod, Superbee, and MC limiters are implemented. These limiters are modifications to the correction that depend on the local behavior of the solution [see LeVeque, 2003, section 6.3; Toro, 2009, section 13.7] and are designed to suppress spurious numerical oscillations that can occur in regions with large gradients in  $q$ , such as the edges of ash clouds. In the presence of large gradients, the limiter reduces the solution to first-order upwind.

[27] These calculations are first carried out in  $x$  (or  $\lambda$ ), then the updated  $Q_{i,j,k}$  is then used in identical calculations in  $y$  (or  $\phi$ ). This dimension-splitting incorporates contributions from the cross-derivative terms of the Taylor series through using the intermediate  $Q_{i,j,k}$  in the calculation along the second dimension.

### 3.1.2. Corner-Transport Upwind

[28] The DCU method with dimension-splitting can introduce splitting errors and exhibit excess numerical diffusion on coarse grids. As an alternative, we have implemented the Corner-transport upwind (CTU) method for solving the horizontal advection equation. With the CTU method, the  $x$  and  $y$  equations are solved in a single step and the fluxes across cell corners are explicitly accounted for. Equation (22) is modified to include fluctuations and higher-order corrections in the  $j$ -direction. The higher-order correction (equation (25)) to the  $i$ -transport is updated with corner fluxes given following [LeVeque, 2003, equation 20.29]. Since there is no splitting of the dimensions, this method is a more direct calculation of the cross-derivatives of the Taylor series, but can be twice as computationally expensive as DCU. We have implemented this technique for the color form of the advection equation in which velocity is assumed to be divergence-free.

### 3.2. Semi-Lagrangian Method

[29] The DCU and CTU methods are traditional, conservative, finite-volume formulations that are useful when careful attention must be paid to strict adherence to conservation laws (e.g., for research investigations or for long-range transport calculations). For urgent, operational forecasting of ash plumes, we have also implemented a semi-Lagrangian (S-L) numerical scheme for the horizontal advection equation.

[30] In the semi-Lagrangian method [Durran, 1999; Karniadakis and Sherwin, 2005], concentrations at  $Q_{i,j,k}^{n+1}$  are calculated by integrating from any point at time  $t = n + 1$  back along streamlines to a point of origin at  $t = n$ . The point of origin will typically be located at any position within a cell and will require an interpolation step (bilinear or bicubic) to determine its initial concentration value. It is in this interpolation step that mass conservation errors are produced. However, back-integration allows time steps to be used that are much larger than allowed by CFL restrictions for explicit integration of the advection equation or the diffusion terms. The order of accuracy of the S-L technique depends on the order of the time-integration scheme for back-calculating along the streamlines, on the order of the interpolation for the velocity field during the back-calculation, and the order of interpolation for the concentration calculation at the origin point at  $t = n$ . We have tested various combinations and found a preferred balance between execution speed and accuracy by using a second-order Runge-Kutta scheme for back-integration, a bilinear interpolant for the velocity field, and using a bicubic interpolation for reconstructing ash concentration at the origin point.

### 3.3. Diffusion

[31] Diffusion is calculated using dimension-splitting with an implicit (Crank-Nicolson) method in each coordinate to keep time steps reasonable. Diffusion can optionally be treated explicitly (Forward Euler) for low diffusivities where diffusion is not the constraining factor on the time step. For several well-documented eruptions (e.g., Eyjafjallajökull, 2010; event 5 of Redoubt 2009; Grímsvötn, 2011) we have

found that a diffusivity of zero often results in model forecasts that agree well with observations.

## 4. Model Verification

[32] To address the performance of the model, we first need to verify that the model accurately calculates the equations we intend to solve. Examining whether or not these equations are a valid representation of the physical process will be deferred to section 5 where we compare model results with data from the 18 August 1992 eruption of Mt. Spurr. To quantify the accuracy of the methods, we test the performance of the model for simplified conditions where analytic solutions are available. We expect that, as we refine the resolution of the computational grid, the numerical solution will converge on the true solution. The rate of convergence of the error as the cell size of computational grid,  $dx$ , is decreased is a measure of the quality of the numerical technique. We quantify “error” by two measures: the  $L_1$ -norm of the quantity  $Q_{\text{true}} - Q_{\text{calc}}$  and the error in mass conservation,  $(M_{\text{true}} - M_{\text{calc}})/M_{\text{true}}$ . We present results from three different tests designed to measure the robustness of the algorithm in different conditions. The first test, advection in a rigidly rotating wind field, quantifies the amount and location of error in a simplified wind field where no deformation is expected. This test measures the ability of the techniques to capture and propagate sharp interfaces in tephra concentration. In the second test, a non-trivial wind field is used that results in a severe distortion of the initial concentration profile. These two tests address just the horizontal advection routines. To verify that the full sequence of steps (equations (13)–(16)) accurately calculate the governing equation (equation (11)) and to quantify any splitting errors, we apply a test case using the method of manufactured solutions.

### 4.1. Advection Test: Rigid Rotation

[33] This test case examines the effect of rigid-body rotation of a concentration profile through one revolution. The initial concentration distribution for a Cartesian grid is given by LeVeque [2003, section 20.8.2] and consists of a cone and box profiles offset from the point of rotation. The wind field is given by  $u(x, y) = 2y$ ,  $v(x, y) = -2x$ , leading to one revolution at  $t = \pi$ . Results for a Cartesian coordinate system are shown in Figure 4. A similar test was conducted in spherical coordinates using the grid shown in Figure 3b. The use of limiters in the DCU and CTU methods (right three plots in Figures 4 (top) and 4 (middle)) significantly improves the quality of the solution. These limiters are invoked in regions of steep gradients, such as the boundaries of the box. Extensive invocation of these limiters reduces the order of convergence of the system to first-order, as can be seen in Figure 8.

[34] Figure 5 compares the execution time for the twelve cases shown in Figure 4. To more clearly distinguish between cases, the times are normalized to the DCU run without limiters. The use of limiters results in a minimal difference in execution time. Using the CTU method, however, can be nearly twice as costly. The semi-Lagrangian method only becomes advantageous for larger CFL-factors, where it can be significantly faster than the DCU method.

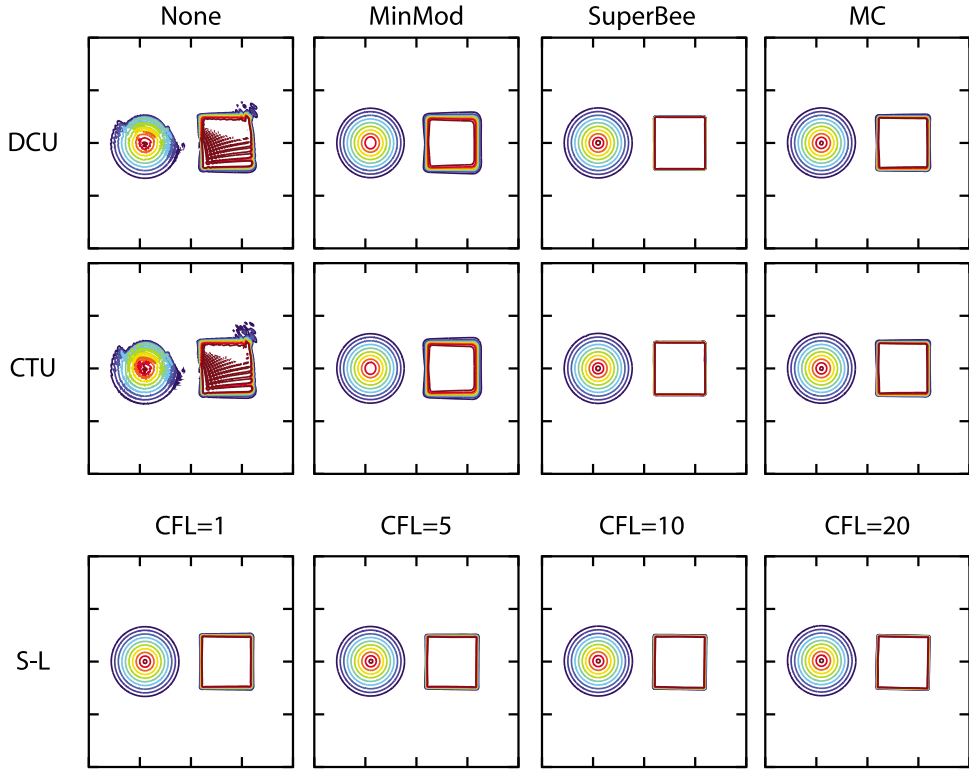


**Figure 4.** Rigid rotation (Cartesian coordinates) of box and cone concentration profiles. The solution at  $t = \pi$  is shown for (top) DCU, (middle) CTU and (bottom) semi-Lagrange. For DCU and CTU schemes, the columns (from left to right) correspond to limiters of: none, minmod, Superbee, and MC. For the semi-Lagrange scheme, the results (from left to right) are for CFL factors of 1, 5, 10, and 20.

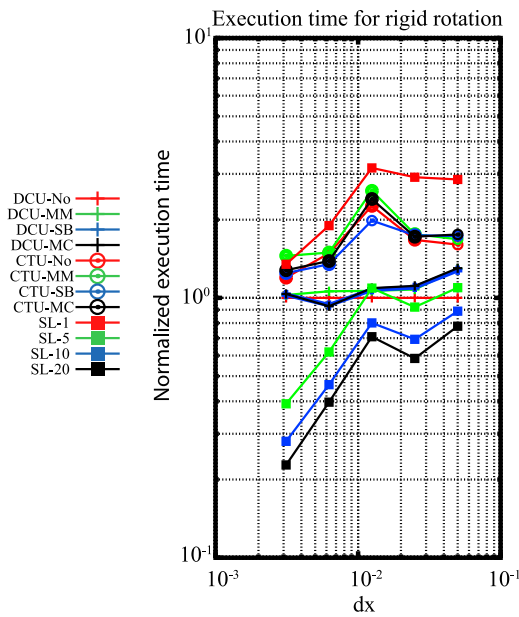


**Figure 5.** Comparison of the execution time for the various methods discussed for the rigid-body circular advection in Cartesian coordinates. The execution time is normalized to the DCU method with no limiter.

#### 4.2. Advection Test: Shear Rotation

[35] To evaluate the ability of these numerical schemes to track advection in highly deforming wind fields, a test was run using a transient, rotational wind field where the rotational velocity about the pole ( $\phi_0 = 0^\circ$ ,  $\lambda_0 = 0^\circ$ ) is given by (shown in Figure 6b)

$$\omega(\phi, \lambda) = -0.5 \sin(d\pi/18)\cos(\pi t/4) \quad (26)$$

where  $d$  is the angular distance (in degrees) of  $\phi, \lambda$  from  $\phi_0, \lambda_0$ . The initial concentration distribution (shown in Figure 6a) is given by

$$q(\lambda, \phi, z, t = 0) = 0.5(1.0 + \cos(\pi r)) \quad (27)$$

where  $r$  is given by:

$$r = \min(1.0, \sqrt{(\phi + 16.0)^2 + \lambda^2}/16) \quad (28)$$

The initial concentration distribution is deformed into a long strand at  $t = 2$  (Figure 6c), then the deformation reverses back to the initial configuration. A similar test in Cartesian coordinates [Durran, 1999, section 5.7.4] was also conducted. Versions of the test cases for both Cartesian and spherical coordinates are shown.

[36] Figure 7 shows the behavior of the various numerical methods for this test problem at  $t = 4$  when the deformation should return to zero. Each plot of Figure 7 should be compared with Figure 6a. Since diffusion is not calculated in

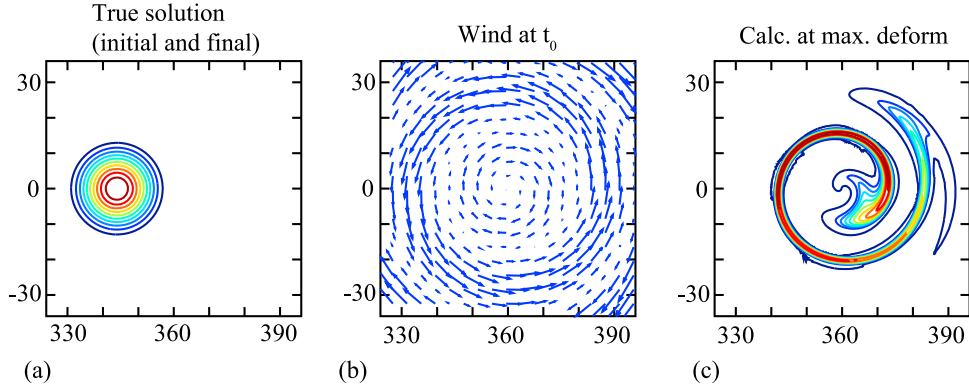


**Figure 6.** Shear test case results using the CTU method with no limiter: (a) the true solution, (b) the windfield at  $t = 0$ , and (c) the calculated solution at  $t = 2.0$  (maximum deformation).

this test problem, any distortion of the final profile is a result of numerical diffusion. The CTU method without the use of a limiter recovers the initial profile with the greatest fidelity. However it is possible in this case, since the use of limiters is non-linear, that errors in the advection in the clock-wise rotation are simply reversed in the counter-clock-wise phase of the oscillation.

[37] Convergence results for both the rigid advection and the shear advection cases are shown in Figure 8. The expressions for the wind fields for both the rigid rotation and

the shear rotation test cases are divergence-free. This is not necessarily true for the discrete approximation of the wind fields. Nevertheless, the CTU implementation (which uses the color equation) performs about as well as the mass-conservative DCU method for the rigid advection test case. Because of the sharp boundary of the concentration and therefore the frequent use of limiters, we see approximately first-order convergence for the rigid rotation test case in both Cartesian and spherical coordinates. The semi-Lagrangian technique converges at about the same rate in the  $L_1$ -norm,

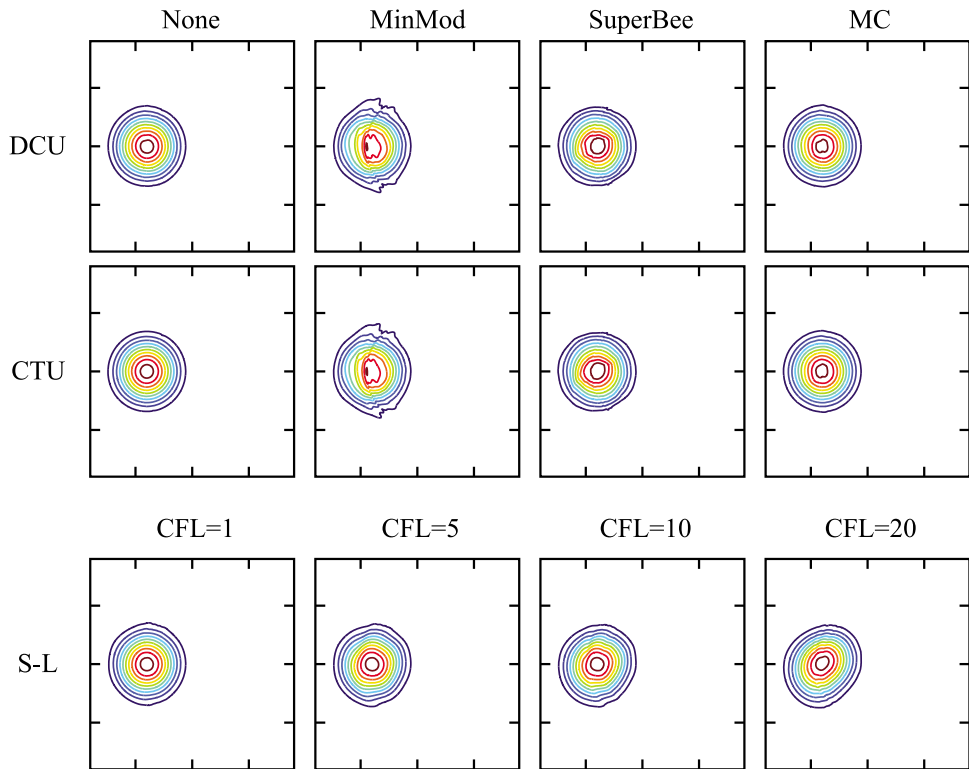


**Figure 7.** Comparison of the solution of the rotational shear test case at  $t = 4.0$  for the various numerical methods. Note that the true solution at this time is the same as the initial distribution (compare with Figure 6a). (top) The solutions for the DCU scheme and (middle) the solutions for the CTU scheme with limiters (from left to right): none, minmod, Superbee, and MC. (bottom) The solutions for the semi-Lagrangian scheme with CFL factors of (from left to right) 1, 5, 10 and 20.

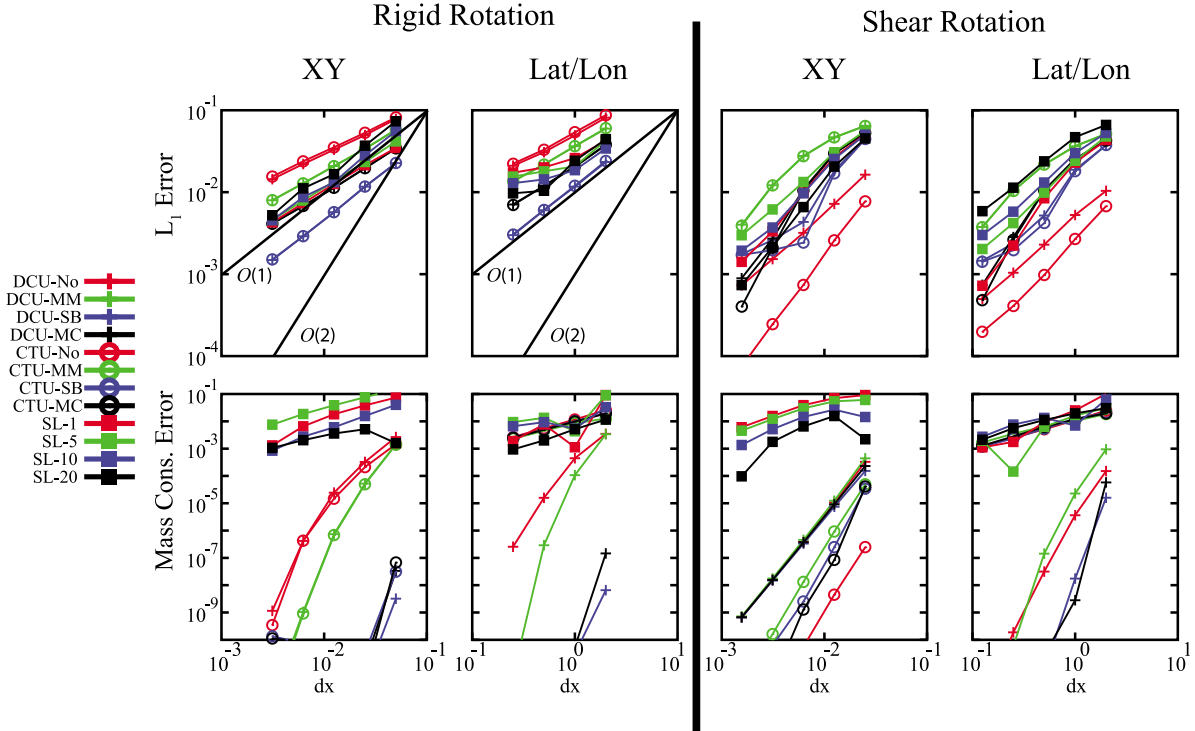


**Figure 8.**  $L_1$  and mass-conservation errors for both the rigid and shear advection for both Cartesian and latitude/longitude coordinates.

but the mass-conservation error is approximately 0.1% per revolution.

[38] For the shear rotation test case, the concentration profile does not have sharp boundaries, resulting in less frequent use of limiters. In this test case, we see slightly less than second-order convergence in the  $L_1$ -norm. Mass conservation is also minimal for the DCU method, but about 0.1% per oscillation for the semi-Lagrangian method.

#### 4.3. Method of Manufactured Solutions

[39] In addition to the two test cases shown above (rotational advection and reversible rotational shear) simple 1-dimensional advection and 1-dimensional diffusion tests were conducted along the coordinate axis to verify convergence properties. Simple tests such as these are useful for identifying obvious bugs in the code; however, they do not fully test all aspects of the algorithm. In general, analytic solutions are not available for the advection-diffusion-sedimentation equation in a non-trivial wind field with realistic pressure and temperature profiles (see Stockie [2011] for solutions in simplified atmospheric conditions). However, the Method of Manufactured Solutions (MMS) [Roache, 2009; Salari and Knupp, 2000] provides some guidance on how to generate analytic solutions for non-trivial atmospheric conditions which will invoke all components of the algorithm, all terms of the governing equation and boundary conditions. This will allow us to confirm the order of accuracy of the complete algorithm.

[40] If a domain is specified and atmospheric and boundary conditions prescribed, then a “source” (a transient spatial distribution of tephra characterizing the eruption) results in a “solution” (a transient spatial distribution of airborne and deposited tephra) through the governing equation.

In equation (11), the source is  $S$  and the solution is  $q$ . In general, we do not know the solution *a priori* that is the result of the source term and boundary conditions. The idea behind the Method of Manufactured Solutions is to find a compatible set of functions for the source and the solution by specifying  $q$  and solving for  $S$ .

[41] To employ the MMS method, we first choose a model geometry (domain and topography) and define the physical state ( $p, T, u, v, w, \mathbf{K}$ ). Next, we simply choose a non-trivial solution,  $q$ , ideally one with a 3-dimensional, transient structure that is easily differentiable. This artificial solution need not be physically realistic since our goal is to evaluate the performance of the algorithm, not model a particular physical process. This solution can be inserted into the governing equation (equation (11)) and evaluated to generate a non-trivial, three-dimensional, transient source term,  $S$ . Note that this source term will not resemble the vertical distribution described in section 2.3, but instead will be a transient three-dimensional function. Initial conditions are generated by simply evaluating the chosen solution at  $t = t_0$ . Boundary conditions can be determined by evaluating  $q$  along the boundary. Applying the algorithm with these initial and boundary conditions, along with the source term, will generate a numerical solution that can be compared with the solution that was initially chosen. Grid convergence studies of this test case will quantify the order of accuracy of the full algorithm.

[42] We use the following domain for the MMS test.  $-100 < x < 100$  km,  $-100 < y < 100$  km,  $0 < z < 20$  km. We use a standard atmosphere for the pressure and temperature profiles given by Wallace and Hobbs [1977, chapter 1]:  $P = P_0 \exp(-z/\delta)$  and  $T = T_0 + \theta z$ . For the wind velocity structure, we adopt a horizontal model to mimic wind shear

**Table 1.** Constants Used in the MMS Test Case

	Value	Units	Description
$d$	100	$\mu\text{m}$	Diameter of grain
$\rho$	2000	$\text{kg/m}^3$	Density of tephra
$F$	0.4		Shape parameter
$g$	9.8	$\text{m/s}^2$	Acceleration of gravity
$R_s$	286.98	$\text{J/kg}^\circ\text{K}$	Specific gas constant of dry air
$\eta_0$	$1.72 \times 10^{-5}$	$\text{Pa/s}$	Reference dynamic viscosity
$T_{ref}$	273.0	$^\circ\text{K}$	Reference temperature for Sutherland's Law
$S$	117.0	$^\circ\text{K}$	Sutherland constant
$P_0$	100	Pa	Pressure at ground surface
$\delta$	7	km	Scale height for pressure
$T_0$	300	$^\circ\text{K}$	Temperature at ground surface
$\theta$	-7	$^\circ\text{K/km}$	Adiabatic lapse rate
$U_0$	10	m/s	Characteristic velocity in $x$
$V_0$	10	m/s	Characteristic velocity in $y$
$W_0$	1	m/s	Characteristic velocity in $z$
$Z_0$	10	km	Height of tropopause
$\lambda_{xy}$	200	km	Horizontal length scale
$\zeta_0$	200	km	Vertical length scale

with small vertical perturbations:  $u = U_0$ ,  $v = V_0$  ( $1 + \tanh(z - Z_0)/2$ ),  $w = -W_0 \cos(\pi x/\lambda_{xy}) \cos(\pi y/\lambda_{xy})$ . The diffusivity is set to a constant. The fall model is set via the equations of section 2.3 using the ideal gas law and Sutherland's Law to calculate  $\rho_a$  and  $\eta_a$ .

[43] The solution we choose is given below.

$$q = Q_0 \operatorname{sech}\left(\frac{x}{\lambda_{xy}}\right) \operatorname{sech}\left(\frac{y}{\lambda_{xy}}\right) \operatorname{sech}\left(\frac{z}{\zeta_0}\right) \quad (29)$$

where  $\zeta = W_0 t + \zeta_0$ . To calculate the source term,  $S$ , we need to calculate the first partial derivatives of  $q$  with respect to  $t$ , and both first and second partial derivatives with respect to the spatial coordinates. The choice of equation (29) is not unique, but is guided by the simple form of the derivatives. Assembling these terms into the governing equation (equation (11)) leads to a simple expression for the source term,  $S$ , which is a continuous function of space and time. By selecting individual constants (i.e.,  $U_0$ ,  $V_0$ ,  $W_0$ ,  $Z_0$ ,  $\zeta_0$ ) we can selectively activate or deactivate branches of the algorithm. If all are activated, we have an analytic solution against which we can compare the full advection-diffusion-sedimentation equation. This is particularly important for calculating splitting errors due to the decomposition of the governing equation via the method of fractional steps. The constants used in the test case are given in Table 1.

[44]  $L_1$ -norm convergence results are shown in Figure 9. The full simulation using the semi-Lagrangian scheme for the horizontal advection produces results that converge with an order accuracy of 1.5. Without the use of limiters, the DCU and CTU schemes converge with second-order accuracy. With minmod, Superbee and MC limiters, the accuracy of the calculations with DCU and CTU for horizontal advection reduces to approximately order 1.8. The fact that these convergence rates are nearly second-order suggests that splitting errors are minimal. Although the use of limiters in this particular case reduces the order of convergence slightly, they significantly improve the resolution of sharp boundaries.

## 5. Model Validation: Mt. Spurr, 1992

[45] The eruptions of the Crater Peak vent of Mt. Spurr in June, August and September of 1992 provide an excellent

test case for validating model results due the ample tephra samples collected, as well as the ground and satellite observations.

[46] Mt. Spurr is an andesitic stratovolcano located in the upper Cook Inlet Region, south central Alaska, approximately 130 km west of Anchorage. Following about 10 months of increased seismicity, the Crater Peak satellitic cone (2309 m) of Mt. Spurr erupted on 27 June 1992 [Eichelberger et al., 1995]. The bulk of the ash from this eruption was distributed northward over the remote Alaska Range. In the following few months, the Crater Peak vent erupted twice more, on 18 August and on 16–17 September. With both of these subsequent eruptions, ash was carried eastward and deposited across southern Alaska. Deposits from both the 18 August and the 16–17 September eruptions were characterized by about 50 measurements of mass per unit area and measurements of the grain size distribution [McGimsey et al., 2001; Durant and Rose, 2009].

[47] We will focus on the 18 August 1992 event for validating the Ash3d model. This eruption commenced at 4:42 p.m. ADT (19/08/1992 00:42 UTC) and sent a subplinian plume to approximately 14 km above sea level. The tephra sample data set is primarily described by Neal et al. [1995], Gardner et al. [1998], and McGimsey et al. [2001]. The total erupted volume was calculated to be  $14 \times 10^6 \text{ m}^3$  DRE [McGimsey et al., 2001]. A total grain size distribution was calculated from sieve analyses conducted by McGimsey et al. [2001] and Durant and Rose [2009]. This grain size distribution is posted as a commissioned data set on the IAVCEI Commission on Tephra Hazard Modeling Web page (IAVCEI).

[48] The primary data that we will be using for validation is the mass per unit area at sample locations. The tephra data set, however, is much richer in that grain size distribution data are available at individual sample locations, enabling a

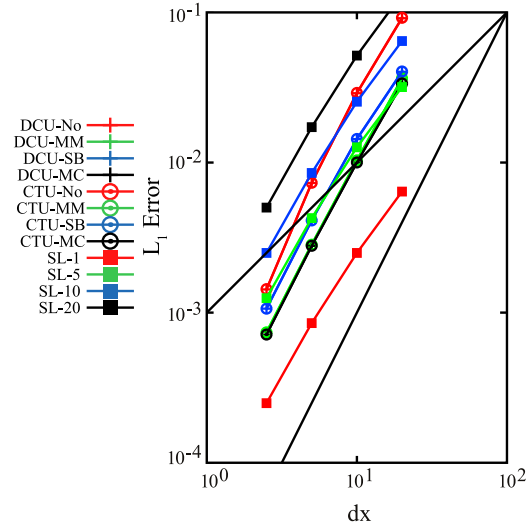


**Figure 9.** Convergence of the MMS test problem in the  $L_1$ -norm. The fastest convergence rates are of order 2.0 for DCU and CTU without limiters. When minmod, Superbee and MC limiters are used, the convergence rate is reduced to order 1.8. For the semi-Lagrangian scheme, the rate of convergence is approximately order 1.5.

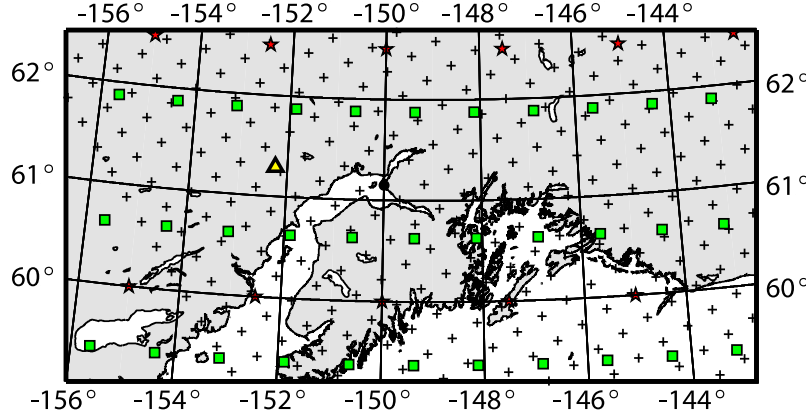


**Figure 10.** Comparison of resolution of the wind data. The native grids for NCEP-NARR (+), NCEP-DOE AMIP-2 (star), NASA-MERRA (square), are shown along with the location of the 1-D radiosonde profile at ANC (circle). The vent location is shown as a triangle.

more detailed study of the evolution of ash-particle size distributions. In addition to ground-based data, AVHRR brightness-temperature difference (BTD) images of the 18 August 1992 event are available [Rose et al., 2001] which can be used to compare with model predictions of airborne ash.

[49] Because the data sets are fairly complete, this eruption has also been well studied using a variety of numerical models such as MDLP0 [Malo and Servranckx, 2007;

Durant and Rose, 2009], Fall3d [Folch et al., 2009], Puff [Searcy et al., 1998], VAFTAD [Heffter and Stunder, 1993], HAZMAP [Folch et al., 2008] and an isentropic trajectory model for SO<sub>2</sub> [Shannon, 1996].

[50] The parameter that is the dominant influence on the location and, to some extent, thickness of a deposit, is the wind field. For the 18 August 1992 eruption, the primary meteorological data are from a radiosonde launched at 19/08/1992 00:00 UTC (42 minutes prior to the eruption)

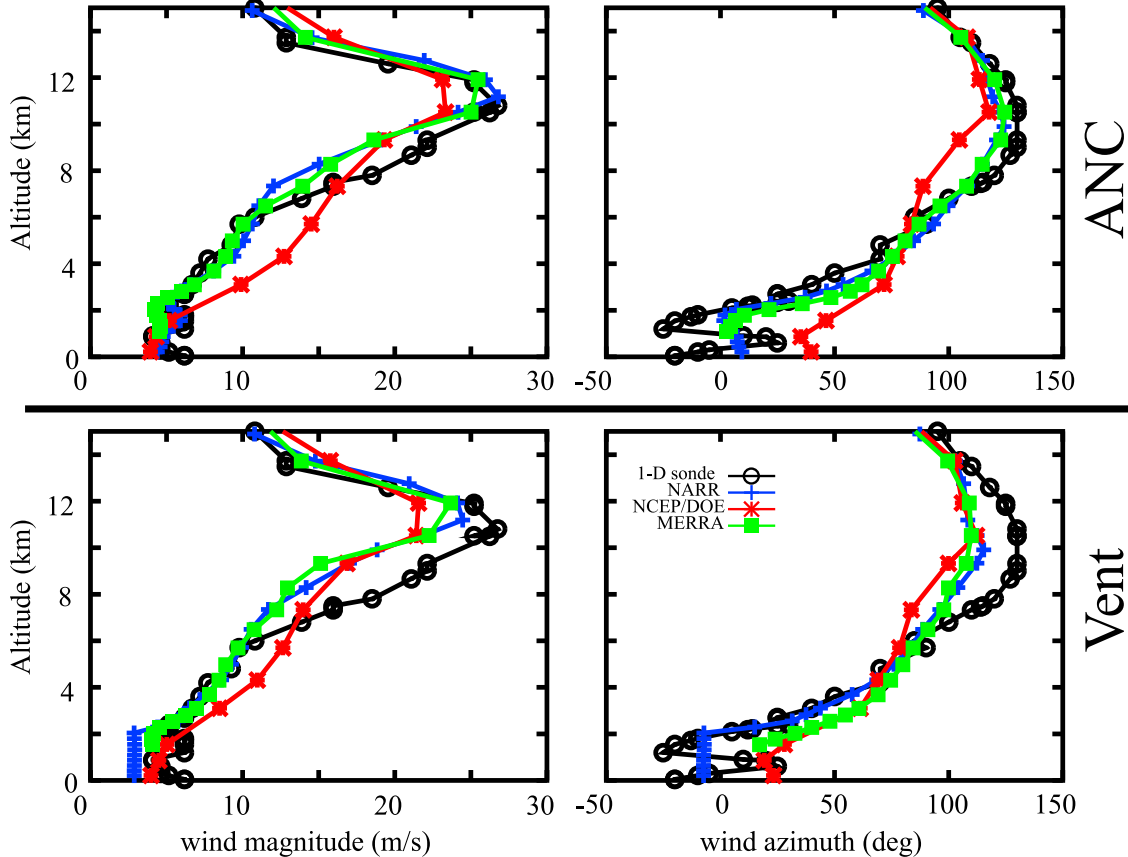


**Figure 11.** The interpolated wind data are compared at the vent and ANC locations.

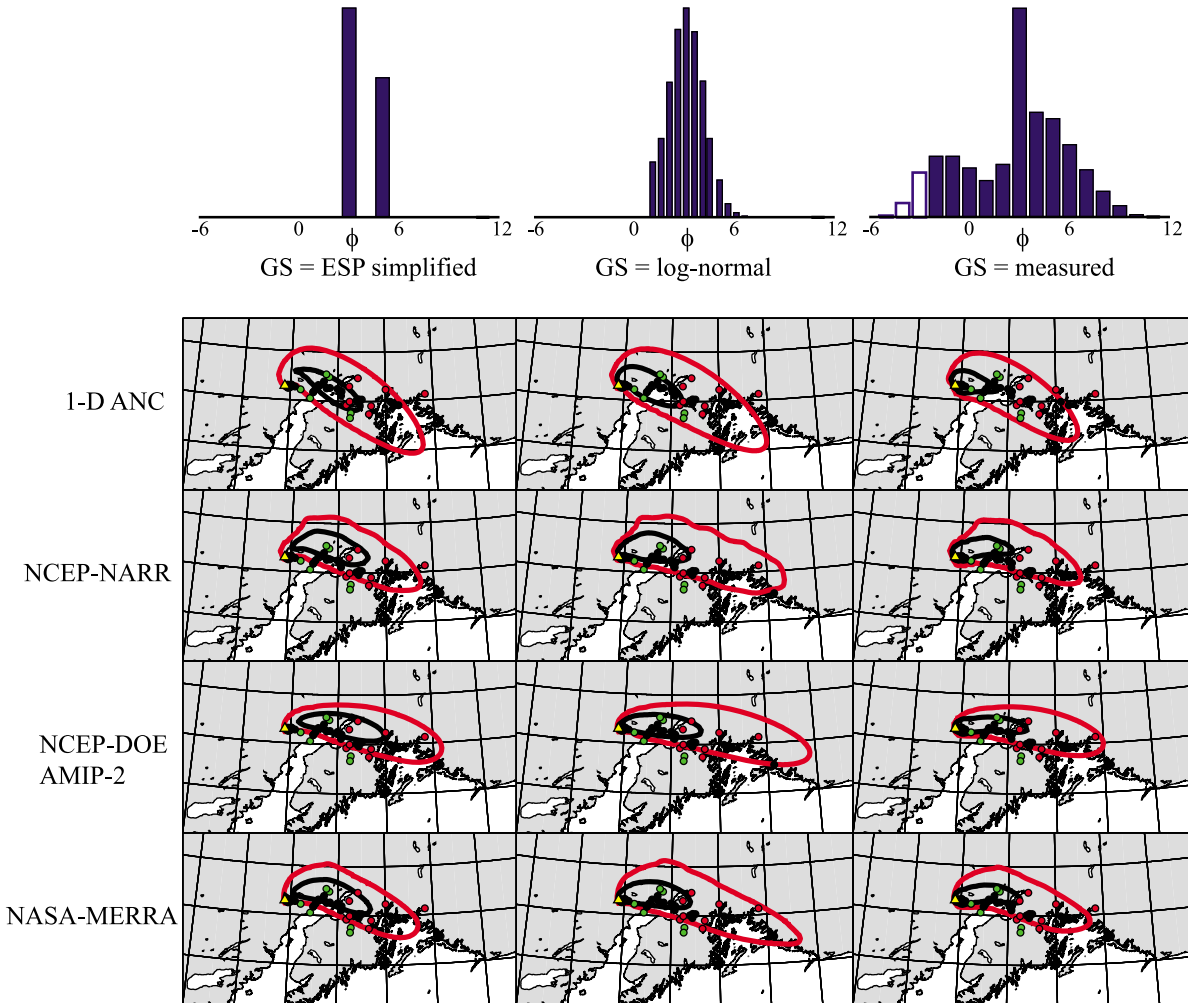


**Figure 12.** Ash3d results for the 18 August 1992 eruption of Crater Peak on Mt. Spurr using four different wind fields and using three grain size distributions. The  $\phi = 3\text{--}5$  (8, 16 and 32 mm) bins of the measured distribution are outlined for reference, however, they were not included in the simulation since they rapidly fall out and required too small of a time step. Simulations do not include topography. Contours of the modeled deposit are 0.1 (red) and 1.0  $\text{kg}/\text{m}^2$  (black). Field data is shown as green ( $< 0.1 \text{ kg}/\text{m}^2$ ), red ( $> 0.1 \text{ kg}/\text{m}^2$  and  $< 1.0 \text{ kg}/\text{m}^2$ ), and black ( $> 1.0 \text{ kg}/\text{m}^2$ ) dots. Grid lines are the same as in Figure 10.

at the Anchorage International Airport (ANC) located approximately 130 km east of the vent. These data are available from the University of Wyoming's radiosonde database (<http://weather.uwyo.edu/upperair/sounding.html>). For regional transport, transient, 3-D numerical weather prediction data are preferable. There are several reanalysis products available for this region. We test three reanalysis products that are freely available: the NCEP North American Regional Reanalysis (NARR [Mesinger *et al.*, 2006]), the NCEP-DOE Atmospheric Model Intercomparison Project (AMIP-2) Reanalysis [Kanamitsu *et al.*, 2002], and NASA's Modern-Era Retrospective analysis for Research and Applications (MERRA) [Rienecker *et al.*, 2011]. The NCEP-NARR data are available on a projected grid at a spatial resolution of 32 km and a temporal resolution of 3 hours. The NCEP-DOE AMIP-2 data are available globally at a spatial resolution of  $2.5^\circ$  and a temporal resolution of 6 hours. The NASA-MERRA data are also globally available, but with a spatial resolution of  $1.25^\circ$  and a temporal resolution of

3 hours. Figure 10 shows the locations of the grid points for each of these reanalysis files for southern Alaska. The spatial resolution of the NCEP-NARR data is significantly greater than for the other two reanalysis products.

[51] Figure 11 shows the wind magnitude and azimuth for the various reanalysis products in comparison to the 1-D sounding at the Anchorage International Airport (ANC). Wind data are interpolated onto the coordinates of ANC and the vent location. None of the reanalysis products capture the rapid change in azimuth observed in the lowest two kilometers. The NCEP-NARR and NASA-MERRA data reproduces the wind speed and azimuth with the greatest fidelity in the elevation ranges of 2–6 km and  $>10$  km, but report a slightly slower wind speed ( $\sim 5 \text{ m/s}$ ) between 6 and 10 km. The NCEP-DOE AMIP-2 data, which is at the coarsest resolution, deviates the greatest from the observations. With the wind data interpolated to the vent location, there is a similar discrepancy among the reanalysis products with low-level wind azimuths differing by up to  $60^\circ$ .

**Table 2.** Input Parameters for the 18 August 1992 Mt. Spurr Simulations

	Parameters
Vent height	2.309 km
$\Delta x$ , $\Delta y$	10 km
$\Delta z$	0.25 km
$K_{x,y,z}$	500 m <sup>2</sup> /s
$k$	8
Start time	19/08/1992 00:42 UTC
Duration	3.5 hours
Plume height	13.7 km
Eruptive vol.	0.014 km <sup>3</sup>
Fall model	WH + slip

[52] To test the sensitivity of the model to the wind and the grain size characterization, we simulated the eruption using the four input wind files (three 3-D reanalysis files and the 1-D sounding) for each of three grain size distributions: the full 17-bin distribution as calculated from the individual sieve analysis (labeled as “measured” in Figure 12), a log-normal distribution (with mean  $\mu_\phi = 3$  and standard deviation  $\sigma_\phi = 1.5$ ) that matches the mean of the measure distribution [Folch et al., 2008] using 14 bins, and a simplified 2-bin grain size distribution using the fraction fine ash from the “S2” characterization of eruption source parameters (ESP) [Mastin et al., 2009] of the volcano (40%) with the remainder as  $d = 0.125$  mm. Normalized histograms of these trial distributions are plotted along the top in Figure 12. For the “measured” grain size distribution, the 8, 16 and 32 mm grain sizes were removed from the simulation since the fall velocities were too fast to be significantly transported and since they required too small of a time step. The execution time roughly scales linearly with the number of grain size bins so the inclusion of the full suite of grain sizes measured adds a significant computational burden compared to the simplified models. The parameters characterizing the eruption are given in Table 2 and the grain size distributions listed in Table 3. In all cases, the shape parameter used was  $F = 0.8$ . The density was assumed to be  $\rho = 800$  kg/m<sup>3</sup> for  $d > 300 \mu\text{m}$ ,  $\rho = 2000$  kg/m<sup>3</sup> for  $d < 88 \mu\text{m}$ , and linearly interpolated for  $88 < d < 300$  [Wilson and Huang, 1979].

[53] This use of the 18 August 1992 Mt. Spurr eruption is not intended to be a thorough investigation of this event, but rather a test of the model’s ability to reproduce observations and to develop a sense of the sensitivity of model predictions on variations in the input parameters. We can see from Figure 12 that 3-D wind fields provide a significant advantage in predicting the tephra deposition pattern. Using the 1-D ANC sounding throughout the modeling domain predicts a deposit axis slightly south of where it was observed for each of the three grain size distributions. Differences of the primary deposit axes (black contour, 1.0 kg/m<sup>2</sup>) using the different 3-D fields are slight although the significant differences in low-level winds do cause some more significant deviations of the low-mpua contour (red, 0.1 kg/m<sup>2</sup>). Differences among the grain size representations in the location of the primary deposit axes are also minor. In fact, the simplified 2-bin grain size distribution performs surprisingly well. Differences in the low-mpua contour are more significant, with the log-normal distribution resulting in deposits that extend farther east than predicted by the simplified model, and in closer alignment with ground observations.

[54] The simulations presented in Figure 12 do not include topographic effects. Anchorage is far enough from the vent (130 km) for the height of the volcano to only play a minor role. Tephra was blown across several mountain ranges east of Anchorage, however, and local topography will play a significant role in the thickness of deposits. Figure 13 shows results from the same set of model runs as in Figure 12, but including topography (GEBCO08 (ICO, 2003)). The GEBCO08 topographic data are at 30 arc-second resolution, which is a much finer resolution than the wind files. Because the low-level winds will be significantly affected by the local topography, it is unlikely to be useful to apply the reanalysis winds using detailed topography. For the model runs shown in Figure 13, the topography was smoothed over a 50 km radius. The inclusion of topography clearly adds more structure to the deposits and results in more isolated pockets of tephra. Broadly speaking, however, the 1.0 kg/m<sup>2</sup> contour is not significantly affected.

[55] In addition to the ground samples of tephra, satellite imagery is available that tracks airborne volcanic ash as well as volcanogenic SO<sub>2</sub> [Rose et al., 2001] using the brightness-temperature difference technique (BTD) [Wen and Rose, 1994; Schneider et al., 1995; Rose et al., 2001]. Figure 14 compares Ash3d results for airborne ash concentration with a 4–5 BTD image from AVHRR at approximately 3 hours after the onset of the eruption. The Ash3d simulation used the NCEP-NARR reanalysis winds with the 14-bin log-normal grain size distribution. The results are vertically integrated to calculate the total mass loading in kg/m<sup>2</sup>. This integration was done over all the grain size bins (thick line in Figure 14a) and over the finest bins corresponding to all ash particles smaller than 20  $\mu\text{m}$  (thin line in Figure 14b). This is the approximate size of ash particles that the BTD technique is most sensitive. The contours indicate the geometry of the airborne ash cloud in comparison to the geometry of the BTD response. Techniques exist for estimating ash loading

**Table 3.** Grain Size Distributions Used for the 18 August 1992 Mt. Spurr Simulations

$\phi$	$d (\mu\text{m})$	Mass Fraction			
		Measured	Truncated	Log-Normal	ESP
-5	32,000	0.002			
-4	16,000	0.016			
-3	8000	0.050			
-2	4000	0.068	0.0730		
-1	2000	0.068	0.0730		
0	1000	0.055	0.0591		
1	500	0.041	0.0440	0.04948	
1.5	353			0.06982	
2	250	0.059	0.0634	0.12045	
2.5	177			0.16708	
3	125	0.233	0.2502	0.18634	0.6
3.5	88			0.16539	
4	62	0.117	0.1257	0.12106	
4.5	44			0.07034	
5	31	0.110	0.1182	0.03286	0.4
5.5	22			0.01242	
6	16	0.081	0.0870	0.00367	
6.5	11			0.00089	
7	8	0.053	0.0569	0.00020	
8	4	0.029	0.0311		
9	2	0.013	0.0140		
10	1	0.003	0.0032		
11	0.5	0.001	0.0011		

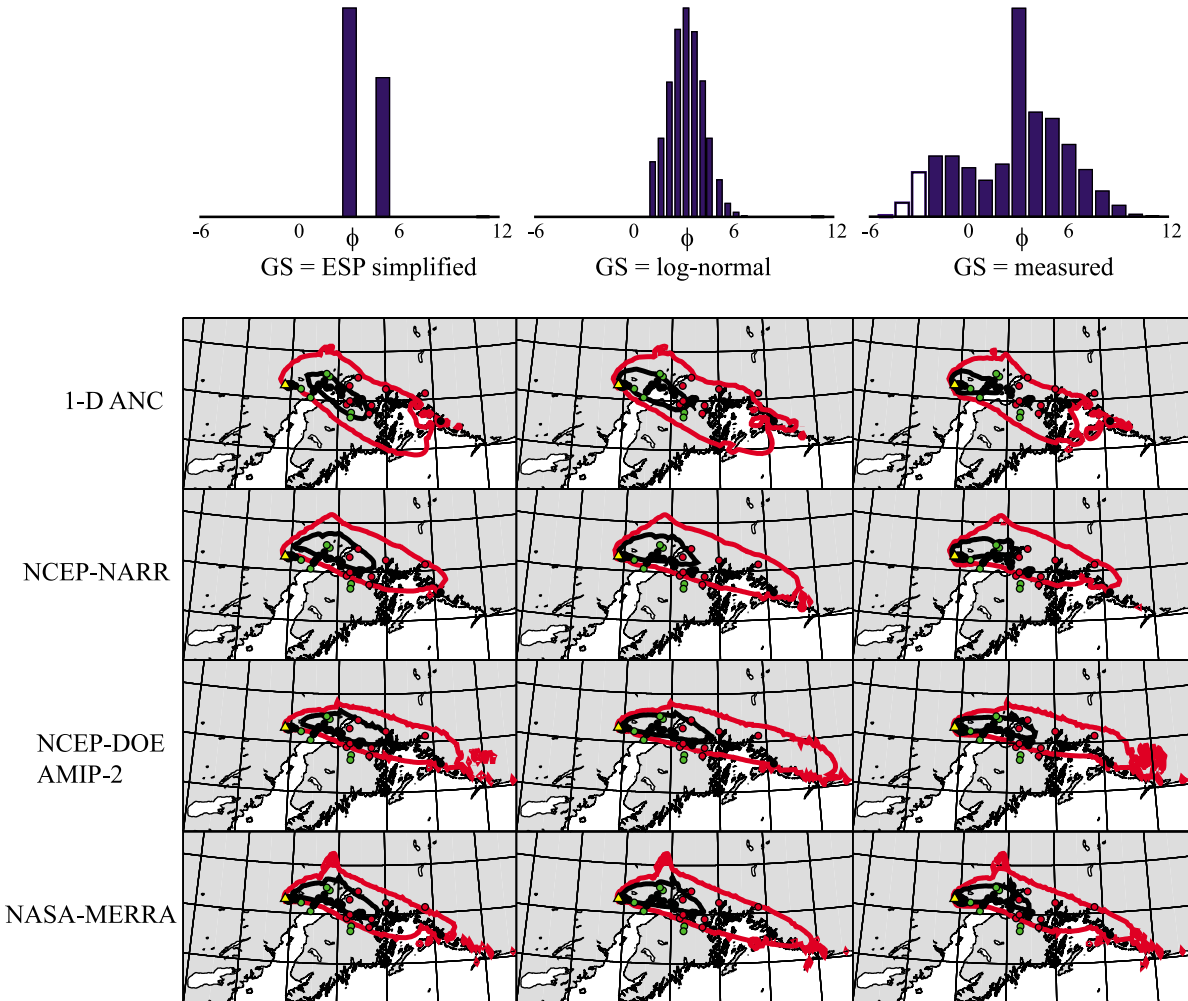


**Figure 13.** Ash3d results for the 18 August 1992 eruption of Crater Peak on Mt. Spurr. Simulations include topography smoothed over 50 km. Contours of the modeled deposit are 0.1 (red) and  $1.0 \text{ kg/m}^2$  (black). Field data is shown as green ( $< 0.1 \text{ kg/m}^2$ ), red ( $> 0.1 \text{ kg/m}^2$  and  $< 1.0 \text{ kg/m}^2$ ), and black ( $> 1.0 \text{ kg/m}^2$ ) dots. Grid lines are the same as in Figure 10.

from these satellite observations [Pavolonis, 2010], however in this study, we only compare ash cloud geometries. In general, as with the comparison to the tephra deposit data, the agreement of the model with satellite data is very encouraging. Both the modeled deposit and airborne ash, however, show a slight trend farther north than was observed in the satellite and ground data. Moreover, calculated deposits cover a larger area than was observed.

[56] To test the sensitivity of the model output to perturbations in model input parameters, numerical experiments were conducted in which several parameters were systematically varied over a realistic range, while holding the other parameters constant. These sensitivity simulations used the NCEP-NARR wind files and the 2-bin ESP grain size characterization. The output calculation against which we measure sensitivity is the deposit thickness at four sample sites located 78, 149, 266 and 368 km downwind from the vent roughly along the deposit axis. Results are shown in Figure 15. For each parameter, a plot showing the trend in deposit thickness as the parameter is varied is shown on

the left, along with map-view plots of the deposit thickness for the minimum and maximum values of the parameter. The vertical line in the deposit thickness plots indicated the default value used.

[57] Particle density was varied from 800–2500  $\text{kg/m}^3$ . This parameter affects the calculated fall velocity of the particle, with denser particles more rapidly falling. The two proximal sites show an increase in mpuia as the particle density increases. With the exception of very short eruption durations, the deposit thickness is fairly insensitive to this parameter. Note that by keeping the eruptive volume fixed and increasing the duration, the mass eruption rate is reduced. The deposit thickness is directly related to the total eruptive volume at all sample points. In general, we expect that any increase in the diffusivity will result in greater transport of airborne ash off-axis, resulting in a thinner deposit. In general, we found that to be true. However, the most proximal and the most distal points show a slight increase in deposit thickness when increasing the diffusivity. The deposit thickness is very sensitive to the height of

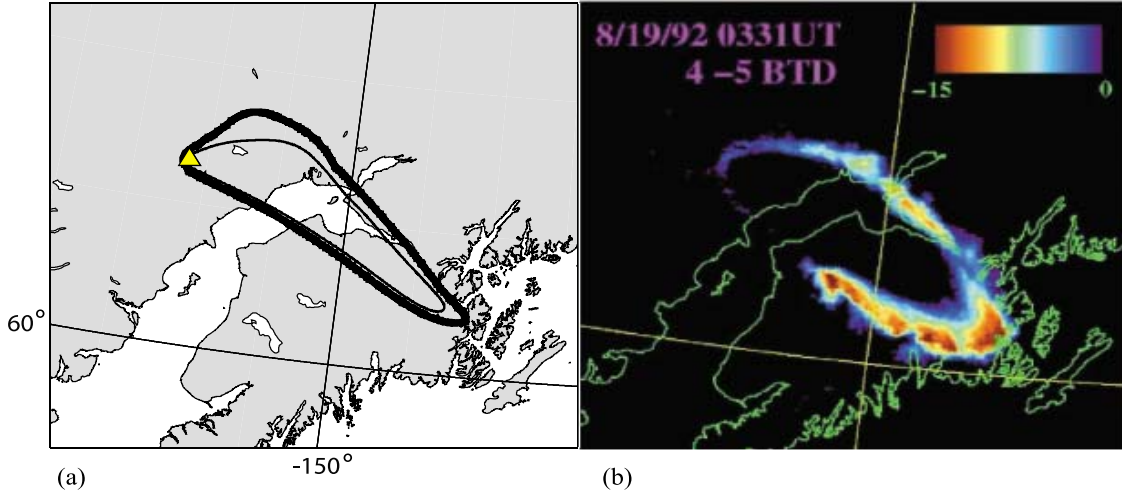


**Figure 14.** Comparison of Ash3d results at 19 August 1992, 3:31 UTC (a) with AVHRR data at 3:31 UTC [Rose *et al.*, 2001]. The contours in Figure 14a correspond to the 1 tonne/km<sup>2</sup> total mass loading of the full grain size distribution (thick line) and the very fine ash fraction (thin line) composed of just particles with  $d < 20 \mu\text{m}$ . (b) The colors indicate greater brightness temperature differences in Band 4 and Band 5 and are interpreted as the edge of the ash cloud (copyright 2001 by The University of Chicago). The core was optically opaque.

the eruption column. The deposits at the most proximal location thin with increasing plume height while the distal sites thicken. The fall model (equation (6)) was fit using data that had an average shape factor of  $F = 0.4$  whereas the Mt. Spurr tephra has a much more equant sphericity [Neal *et al.*, 1995; Riley *et al.*, 2003]. Varying  $F$  from 0.2 to 1.0 has an effect similar to varying density, as increasing  $F$  increases the fall velocity. The direction of the wind at the vent rotated slightly counter-clockwise near the time of the eruption. To test how sensitive results are to the start time of the eruption, the start time was varied from 19/08/1992 00:00 to 19/08/1992 01:30 UTC. The model is fairly insensitive to this parameter. The Suzuki parameter ( $k$ ) controls the vertical distribution of ash in the column, with low values corresponding to a nearly uniform distribution, and higher values corresponding to a more top-heavy distribution. Shifting mass toward the top of the column, in general, causes the very proximal deposits to thin and the distal deposits to thicken. For the sites chosen, all deposits thickened.

[58] The dominant parameter in this list that controls the thickness of the deposit is the total eruptive volume which can span orders of magnitude and will not be known *a priori*. Perturbations to this parameter cause simple scaling of the deposit thickness. This will not be the case for non-linear effects such as wet deposition and aggregation, however for the present algorithm, the scaling is linear. Modifying the remaining parameters will also modify the geometry of the deposit. The most sensitive of the remaining parameters are the plume height and the Suzuki parameter characterizing the eruptive column. Calculated mpua is also surprisingly sensitive to the tephra characterization (density and shape). It should be noted that in these sensitivity tests only individual parameters for a constant eruption are perturbed. Predicted mpua will also be sensitive to transient variations of these parameters over the course of the eruption,

such as plume height [Mastin *et al.*, 2010; Webster *et al.*, 2012].

## 6. Discussion and Conclusions

[59] We have presented a new model for tephra dispersion and sedimentation using a finite-volume framework. Within this framework, we have implemented three numerical schemes which span a spectrum of accuracy and speed. Our simulations show that using the semi-Lagrangian technique for horizontal advection results in an algorithm that converges at a rate of approximately order 1.5. Errors in mass conservation are modest and the execution speed is several times faster than the DCU and CTU methods. In stochastic simulations, which require dozens to hundreds of runs, these advantages prove useful. However, we have found that for real, complex wind fields, the mass-conservative DCU method with dimension splitting using a Superbee flux limiter generates the most reliable results [Mastin *et al.*, 2012]. Our implementation of this method results in an algorithm with a rate of convergence of approximately order 1.8.

[60] In addressing the 18 August 1992 eruption of Mt. Spurr, the model performs well in reproducing the observations, both for deposit calculations and for tephra cloud trajectory. We have begun to identify the primary sensitivities of the model. Of the model input parameters, the dominant sensitivity is to the wind field. For the Mt. Spurr eruption, we found that the 1-D wind profile resulted in tephra deposit predictions that differed the greatest from observations compared to 3-D wind files. Despite the large discrepancy in resolution among the 3-D, transient reanalysis wind files, each adequately predicted the resulting deposit with minor differences among the formats. Surprisingly, the model results were also fairly insensitive to the particular grain size distribution used, of the three described in section 5. Each of these distributions has a peak near  $\phi = 3$ . For parameters characterizing the eruption, the

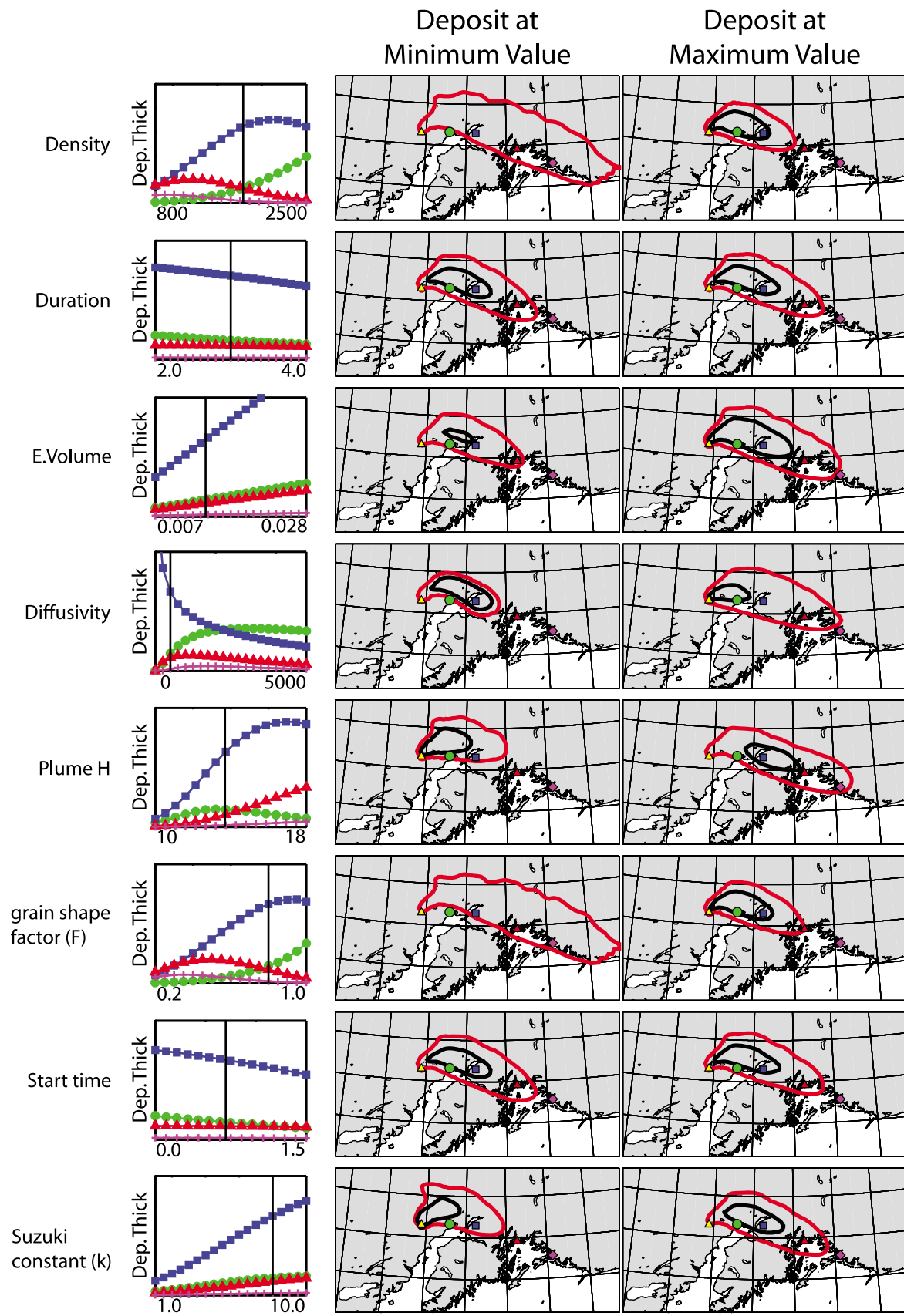


**Figure 15.** Sensitivity of calculated deposit thickness with respect to model input parameters. Results are shown for deposit calculations at 78, 149, 266, and 368 km from the vent. Default values for these parameters are shown as a vertical black line in the plots. Grid lines are the same as in Figure 10.

deposit thickness is most sensitive to the total volume of the eruption, a parameter that can only be estimated during an eruptive event. The next most sensitive parameters are those specifying the vertical distribution of tephra in the eruption column (plume height and Suzuki parameter). These parameters can be estimated in real-time if observations are available (radar, satellite, pilot reports, seismic network). Finally, the parameters controlling the terminal velocity of the tephra particles of a given size can play a significant role (shape factor, density). The model was fairly insensitive to start time and duration (eruptive volume held constant) which is likely due to the slow rate of change of the wind field over the course of the eruption and deposition. It should be noted that comments on these sensitivities are limited to the specific case of the 18 August 1992 eruption of Mt. Spurr, using a simple source characterization and comparing with deposit total mpua. Broader conclusions regarding model sensitivities would require a more comprehensive study using mpua of the individual grain sizes, transient source parameters, higher-resolution wind fields, and non-linear processes such as wet deposition and aggregation.

## Notation

- $x, y, z$  Cartesian coordinate directions.
- $\lambda, \phi, z$  Spherical coordinate directions (longitude, latitude, altitude).
- $q$  Tephra concentration.
- $q^*, q^{**}, q^{***}$  Tephra concentration at fractional steps.
- $t$  Time.
- $\mathbf{u}, u, v, w$  Wind velocity (vector and components).
- $\mathbf{v}_s, v_s$  Fall velocity (vector and scalar)
- $u', \bar{u}$  Perturbation, ensemble average of  $u$ .
- $\mathbf{K}, K_x, K_y, K_z$  Turbulent Diffusivity (tensor, components).
- $S$  Source (emission) rate.
- $d$  Diameter of grain.
- $\rho, \rho_d$  Density of ash particle, deposit.
- $a, b, c$  Major, intermediate, minor axes of ellipsoid.
- $F$  Shape factor.
- $\rho_a$  Density of air.
- $\eta_a$  Dynamic viscosity of air.
- $\lambda_a$  Mean free path of an air molecule.
- $g$  Acceleration of gravity.
- $C_d$  Drag coefficient.
- $C_c$  Cunningham slip-flow correction factor.
- $\alpha, \beta, \gamma$  Slip-flow parameters.
- $Kn$  Knudsen number.
- $Re$  Reynolds number.
- $M_B$  Molecular weight of dry air.
- $R$  Ideal gas constant.
- $P, P_0$  Pressure, Pressure at ground surface.
- $T, T_0$  Temperature, Temperature at ground surface.
- $\delta$  Scale height.
- $\theta$  Adiabatic lapse rate.
- $k$  Suzuki parameter.
- $H$  Plume height.
- $V$  Eruptive volume.
- $Q_{i,j,k}^n$  Average concentration in cell  $i, j, k$  at time  $n$ .
- $\Delta\kappa$  Volume of cell (capacity).
- $F_{i-1/2,j,k}^n$  Flux across interface  $i - 1/2$  at time  $n$ .
- $\sigma_{i-1/2,j,k}$  Area of interface of cell  $i, j, k$ .
- $\mathcal{A}^\pm$  Fluctuation.

- $\tilde{F}_{i-1/2,j,k}$  High-order correction to fluctuation.
- $\Delta Q_{i-1/2,j}$  Limited wave at  $i - 1/2$ .
- $\omega$  Rotational velocity.
- $\lambda_0, \phi_0$  Pole of rotation.
- $L_1$  Error norm.
- $U_0, V_0, W_0$  Characteristic velocity in  $x, y, z$ .
- $Z_0$  Height of tropopause.
- $\lambda_{xy}$  Horizontal length scale.
- $\zeta, \zeta_0$  Transient length scale, characteristic length scale.
- $Q_0$  Characteristic initial concentration.

[61] **Acknowledgments.** Funding for this study has been provided by the U.S. Geological Survey through the Mendenhall Research Fellowship Program and the Volcano Hazards Program. This manuscript was greatly improved thanks to helpful comments from Dave George, Kristi Wallace, John Power, Chris Waythomas, and two anonymous reviewers. The NCEP-NARR data for this study are from the Research Data Archive (RDA), which is maintained by the Computational and Information Systems Laboratory (CISL) at the National Center for Atmospheric Research (NCAR). NCAR is sponsored by the National Science Foundation (NSF). The original NCEP-NARR data are available from the RDA (<http://dss.ucar.edu>) in data set number ds608.0. NCEP-DOE AMIP-II reanalysis (R2) was produced with the support of the U.S. National Weather Service and of PCMDI (U.S. Department of Energy). MERRA data used in this study have been provided by the Global Modeling and Assimilation Office (GMAO) at NASA Goddard Space Flight Center through the NASA GES DISC online archive.

## References

- Armienti, P., G. Macedonio, and M. T. Pareschi (1988), A numerical model for simulation of tephra transport and deposition: Applications to May 18, 1980, Mount St. Helens eruption, *J. Geophys. Res.*, 93(B6), 6463–6476, doi:10.1029/JB093iB06p06463.
- Barsotti, S., A. Neri, and J. S. Scire (2008), The VOL-CALPUFF model for atmospheric ash dispersal: 1. Approach and physical formulation, *J. Geophys. Res.*, 113, B03208, doi:10.1029/2006JB004623.
- Bird, R., W. E. Stewart, and E. N. Lightfoot (1960), *Transport Phenomena*, John Wiley, New York.
- Bonadonna, C., C. Connor, B. Houghton, L. Connor, M. Byrne, A. Laing, and T. Hincks (2005), Probabilistic modeling of tephra dispersion: Hazard assessment of a multi-phase eruption at Tarawera, New Zealand, *J. Geophys. Res.*, 110, B03203, doi:10.1029/2003JB002896.
- Bonadonna, C., A. Folch, S. Loughlin, and H. Puempel (2011), Ash dispersal forecast and civil aviation workshop, consensual document, Univ. of Geneva, Geneva, Switzerland. [Available at <https://vhub.org/resources/503>.]
- Carey, S. N. (1996), Modeling of tephra fallout from explosive eruptions, in *Monitoring and Mitigation of Volcano Hazards*, edited by R. Scarpa and R. I. Tilling, pp. 429–461, Springer, Berlin.
- Casadevall, T. J. (1994), Volcanic ash and aviation safety: Proceedings of the First International Symposium on Volcanic Ash and Aviation Safety, *U.S. Geol. Surv. Bull.*, 2047, 450 pp.
- Chen, B., R. Irwin, Y. Cheng, M. Hoover, and H. Yeh (1993), Aerodynamic behavior of fiber- and disc-like particles in a Millikan cell apparatus, *J. Aerosol Sci.*, 24(2), 181–195, doi:10.1016/0021-8502(93)90057-G.
- Connor, C., B. Hill, B. Winfrey, N. Franklin, and P. LaFemina (2001), Estimation of volcanic hazards from tephra fallout, *Nat. Hazards Rev.*, 2(1), 33–42, doi:10.1061/(ASCE)1527-6988(2001)2:1(33).
- Costa, A., G. Macedonio, and A. Folch (2006), A three-dimensional Eulerian model for transport and deposition of volcanic ashes, *Earth Planet. Sci. Lett.*, 241, 634–647, doi:10.1016/j.epsl.2005.11.019.
- Dacre, H. F., et al. (2011), Evaluating the structure and magnitude of the ash plume during the initial phase of the 2010 Eyjafjallajökull eruption using lidar observations and NAME simulations, *J. Geophys. Res.*, 116, D00U03, doi:10.1029/2011JD015608.
- Dahneke, B. E. (1973), Slip correction factors for nonspherical bodies—III The form of the general law, *J. Aerosol Sci.*, 4(2), 163–170, doi:10.1016/0021-8502(73)90067-0.
- D'Amours, R., and A. Malo (2004), A zeroth order Lagrangian particle dispersion model MLDPO, technical report, Environ. Emerg. Response Sect., Can. Meteorol. Cent., Meteorol. Serv. of Can., Ottawa.
- Draxler, R. R., and G. Hess (1997), Description of the Hysplit-4 modeling system, *Tech. Memo. ERL ARL-224*, Air Resource Laboratory, NOAA, Silver Spring, Md.

- Durant, A. J., and W. I. Rose (2009), Sedimentological constraints on hydrometeor-enhanced particle deposition: 1992 eruptions of Crater Peak, Alaska, *J. Volcanol. Geotherm. Res.*, 186, 40–59, doi:10.1016/j.jvolgeores.2009.02.004.
- Durran, D. R. (1999), *Numerical Methods for Wave Equations in Geophysical Fluid Dynamics, Texts Appl. Math.*, vol. 32, Springer, Berlin.
- Eichelberger, J. C., T. E. C. Keith, T. P. Miller, and C. J. Nye (1995), The 1992 eruptions of Crater Peak Vent, Mount Spurr Volcano, Alaska: Chronology and summary, in *The 1992 Eruptions of Crater Peak Vent, Mount Spurr Volcano, Alaska*, edited by T. E. C. Keith, *U.S. Geol. Surv. Bull.*, 2139, 1–18.
- Folch, A., A. Costa, and G. Macedonio (2008), *HAZMAP Computer Code and Related Documentation*, user's manual, Ist. Naz. di Geofis. e Vulcanol., Napoli, Italy.
- Folch, A., A. Costa, and G. Macedonio (2009), FALL3D: A computational model for transport and deposition of volcanic ash, *Comput. Geosci.*, 35(6), 1334–1342, doi:10.1016/j.cageo.2008.08.008.
- Ganser, G. H. (1993), A rational approach to drag prediction of spherical and nonspherical particles, *Powder Technol.*, 77(2), 143–152, doi:10.1016/0032-5910(93)80051-B.
- Gardner, C. A., K. V. Cashman, and C. A. Neal (1998), Tephra-fall deposits from the 1992 eruption of Crater Peak, Alaska: Implications of clast textures for eruptive processes, *Bull. Volcanol.*, 59(8), 537–555, doi:10.1007/s004450050208.
- Heffter, J., and B. Stunder (1993), Volcanic Ash Forecast Transport And Dispersion (VAFTAD) model, *Weather Forecast.*, 8(4), 534–541, doi:10.1175/1520-0434(1993)008<0533:VAFTAD>2.0.CO;2.
- Jacobson, M. Z. (2005), *Fundamentals of Atmospheric Modeling*, 2nd ed., Cambridge Univ. Press, Cambridge, U. K.
- Jones, A., D. Thomson, M. Hort, and B. Devenish (2007), The U.K. Met Office's Next-Generation Atmospheric Dispersion Model, NAME III, in *Air Pollution Modeling and Its Application XVII*, edited by C. Borrego and A. L. Norman, pp. 580–589, Springer, New York, doi:10.1007/978-0-387-68854-1\_62.
- Josse, B., P. Simon, and V.-H. Peuch (2004), Radon global simulations with the multiscale chemistry and transport model MOCAGE, *Tellus, Ser. B*, 56(4), 339–356, doi:10.1111/j.1600-0889.2004.00112.x.
- Kanamitsu, M., W. Ebisuzaki, J. Woollen, S.-K. Yang, J. H. Hnilo, M. Fiorino, and G. L. Potter (2002), NCEP–DOE AMIP-II Reanalysis (R-2), *Bull. Am. Meteorol. Soc.*, 83(11), 1631–1643, doi:10.1175/BAMS-83-11-1631.
- Karniadakis, G. E., and S. J. Sherwin (2005), *Spectral/hp Element Methods for Computational Fluid Dynamics*, 2nd ed., Oxford Univ. Press, New York.
- Langmann, B., M. Hort, and T. Hansteen (2009), Meteorological influence on the seasonal and diurnal variability of the dispersion of volcanic emissions in Nicaragua: A numerical model study, *J. Volcanol. Geotherm. Res.*, 182(1), 34–44, doi:10.1016/j.jvolgeores.2009.01.031.
- Langmann, B., K. Zakek, and M. Hort (2010), Atmospheric distribution and removal of volcanic ash after the eruption of Kasatochi Volcano: A regional model study, *J. Geophys. Res.*, 115, D00L06, doi:10.1029/2009JD013298.
- LeVeque, R. J. (1996), High-resolution conservative algorithms for advection in incompressible flow, *SIAM J. Numer. Anal.*, 33(2), 627–665, doi:10.1137/0733033.
- LeVeque, R. J. (2003), *Finite Volume Methods for Hyperbolic Problems*, Cambridge Univ. Press, Cambridge, U. K.
- Macedonio, G., A. Costa, and A. Longo (2005), A computer model for volcanic ash fallout and assessment of subsequent hazard, *Comput. Geosci.*, 31(7), 837–845, doi:10.1016/j.cageo.2005.01.013.
- Malo, A., and R. Servranckx (2007), Atmospheric long-range transport and dispersion modeling of August 1992 eruption of Mount Spurr, Alaska, technical report, Environ. Emerg. Response Sect., Can. Meteorol. Cent., Meteorol. Serv. of Can., Ottawa.
- Mastin, L., et al. (2009), A multidisciplinary effort to assign realistic source parameters to models of volcanic ash-cloud transport and dispersion during eruptions, *J. Volcanol. Geotherm. Res.*, 186, 10–21, doi:10.1016/j.jvolgeores.2009.01.008.
- Mastin, L. G., R. P. Denlinger, and H. Schwaiger (2010), Why do models predict such large ash clouds? An investigation using data from the Eyjafjallajökull eruption, Iceland, paper presented at Conference on Eyjafjallajökull and Aviation, Keilir, Keflavik, Iceland, Sept 15–16.
- Mastin, L. G., H. Schwaiger, D. Schneider, K. Wallace, J. Schaefer, and R. Denlinger (2012), Injection, transport, and deposition of ash during event 5 at Mount Redoubt, March 23, 2009, *J. Volcanol. Geotherm. Res.*, in press.
- McGimsey, R. G., C. A. Neal, and C. M. Riley (2001), Areal distribution, thickness, mass, volume, and grain size of tephra-fall deposits from the 1992 eruptions of Crater Peak vent, Mt. Spurr Volcano, Alaska, *U.S. Geol. Surv. Open File Rep.*, 2001-370.
- Mesinger, F., et al. (2006), North American Regional Reanalysis, *Bull. Am. Meteorol. Soc.*, 87(3), 343–360, doi:10.1175/BAMS-87-3-343.
- Neal, C. A., R. G. McGimsey, C. A. Gardner, M. L. Harbin, and C. J. Nye (1995), Tephra-fall deposits from the 1992 eruptions of Crater Peak, Mount Spurr Volcano, Alaska: A preliminary report on distribution, stratigraphy, and composition, in *The 1992 Eruptions of Crater Peak Vent, Mount Spurr Volcano, Alaska*, edited by T. E. C. Keith, *U.S. Geol. Surv. Bull.*, 2139, 65–79.
- Oberhuber, J. M., M. Herzog, H.-F. Graf, and K. Schwanke (1998), Volcanic plume simulation on large scales, *J. Volcanol. Geotherm. Res.*, 87, 29–53, doi:10.1016/S0377-0273(98)00099-7.
- Pavlonis, M. J. (2010), Advances in extracting cloud composition information from spaceborne infrared radiances—A robust alternative to brightness temperatures. Part I: Theory, *J. Appl. Meteorol. Climatol.*, 49(9), 1992–2012, doi:10.1175/2010JAMC2433.1.
- Peterson, R. A., and K. G. Dean (2008), Forecasting exposure to volcanic ash based on ash dispersion modeling, *J. Volcanol. Geotherm. Res.*, 170, 230–246, doi:10.1016/j.jvolgeores.2007.10.003.
- Pfeiffer, T., A. Costa, and G. Macedonio (2005), A model for the numerical simulation of tephra fall deposits, *J. Volcanol. Geotherm. Res.*, 140, 273–294, doi:10.1016/j.jvolgeores.2004.09.001.
- Prata, A. J. (2009), Satellite detection of hazardous volcanic clouds and the risk to global air traffic, *Nat. Hazards*, 51(2), 303–324, doi:10.1007/s11069-008-9273-z.
- Rienecker, M., et al. (2011), MERRA—NASA's modern-era retrospective analysis for research and applications, *J. Clim.*, 24(14), 3624–3648, doi:10.1175/JCLI-D-11-00015.1.
- Riley, C. M., W. I. Rose, and G. J. S. Bluth (2003), Quantitative shape measurements of distal volcanic ash, *J. Geophys. Res.*, 108(B10), 2504, doi:10.1029/2001JB000818.
- Roache, P. J. (2009), *Fundamentals of Verification and Validation*, 2nd ed., Hermosa Publ., Socorro, N. M.
- Rose, W., and A. Durant (2009), Fine ash content of explosive eruptions, *J. Volcanol. Geotherm. Res.*, 186, 32–39, doi:10.1016/j.jvolgeores.2009.01.010.
- Rose, W. I., G. J. S. Bluth, D. J. Schneider, G. G. J. Ernst, C. M. Riley, L. J. Henderson, and R. G. McGimsey (2001), Observations of volcanic clouds in their first few days of atmospheric residence: The 1992 eruptions of Crater Peak, Mount Spurr Volcano, Alaska, *J. Geol.*, 109(6), 677–694, doi:10.1086/323189.
- Salari, K., and P. Knupp (2000), Code verification by the Method of Manufactured Solutions, *Tech. Rep. SAND2000-1444*, Sandia Natl. Lab., Washington, D. C.
- Schneider, D. J., W. I. Rose, and L. Kelley (1995), Tracking of 1992 eruption clouds from Crater Peak Vent of Mount Spurr Volcano, Alaska, using AVHRR, in *The 1992 Eruptions of Crater Peak Vent, Mount Spurr Volcano, Alaska*, edited by T. E. C. Keith, *U.S. Geol. Surv. Bull.*, 2139, 27–36.
- Searcy, C., K. Dean, and W. Stringer (1998), PUFF: A high-resolution volcanic ash tracking model, *J. Volcanol. Geotherm. Res.*, 80(1), 1–16, doi:10.1016/S0377-0273(97)00037-1.
- Seinfeld, J. H., and S. N. Pandis (2006), *Atmospheric Chemistry and Physics: From Air Pollution to Climate Change*, 2nd ed., Wiley-Intersci., Hoboken, N. J.
- Shannon, J. M. (1996), 3-d reconstruction of the Mt. Spurr volcanic clouds using AVHRR, TOMS, and wind trajectory data, MS thesis, Mich. Technol. Univ., Houghton.
- Sparks, R. S. J., M. I. Bursik, S. N. Carey, J. S. Gilbert, L. S. Glaze, H. Sigurdsson, and A. W. Woods (1997), *Volcanic Plumes*, John Wiley, Chichester, U. K.
- Steensen, T. S., M. Stuefer, P. Webley, G. A. Grell, and S. R. de Freitas (2010), Analysis of the Eyjafjallajökull eruption using the WRF-Chem model compared to satellite-based ash retrieval algorithms, Abstract V41E-2320 presented at 2010 Fall Meeting, AGU, San Francisco, Calif., 13–17 Dec.
- Stockie, J. M. (2011), The mathematics of atmospheric dispersion modeling, *SIAM Rev.*, 53(2), 349–372, doi:10.1137/10080991X.
- Stohl, A., C. Forster, A. Frank, P. Seibert, and G. Wotawa (2005), Technical note: The Lagrangian particle dispersion model FLEXPART version 6.2, *Atmos. Chem. Phys.*, 5(9), 2461–2474, doi:10.5194/acp-5-2461-2005.
- Suzuki, T. (1983), A theoretical model for dispersion of tephra, in *Arc Volcanism: Physics and Tectonics*, edited by D. Shimozuru and I. Yokoyama, pp. 95–113, Terra Sci., Tokyo.
- Toro, E. F. (2009), *Riemann Solvers and Numerical Methods for Fluid Dynamics: A Practical Introduction*, 3rd ed., Springer, Dordrecht, Netherlands.
- Wallace, J. M., and P. V. Hobbs (1977), *Atmospheric Science: An Introductory Survey*, Academic, New York.

- Webster, H. N., et al. (2012), Operational prediction of ash concentrations in the distal volcanic cloud from the 2010 Eyjafjallajökull eruption, *J. Geophys. Res.*, 117, D00U08, doi:10.1029/2011JD016790.
- Wen, S., and W. I. Rose (1994), Retrieval of sizes and total masses of particles in volcanic clouds using AVHRR bands 4 and 5, *J. Geophys. Res.*, 99(D3), 5421–5431, doi:10.1029/93JD03340.
- Westphal, D. L., H. Chen, J. R. Campbell, K. Richardson, J. D. Doyle, and M. D. Fromm (2008), Numerical investigation and forecasting of the Kasatochi ash plume, *Eos Trans. AGU*, 89(53), Fall Meeting Suppl., Abstract >A53B-0267.
- Wilson, L., and T. C. Huang (1979), The influence of shape on the atmospheric settling velocity of volcanic ash particles, *Earth Planet. Sci. Lett.*, 44(2), 311–324, doi:10.1016/0012-821X(79)90179-1.
- 
- R. P. Denlinger and L. G. Mastin, Cascades Volcano Observatory, U.S. Geological Survey, 1300 SE Cardinal Ct., Ste. 100, Vancouver, WA 98686, USA. (roger@usgs.gov; lgmastin@usgs.gov)
- H. F. Schwaiger, Alaska Volcano Observatory, U.S. Geological Survey, 4210 University Dr., Anchorage, AK 99508, USA. (hschwaiger@usgs.gov)